

Early ultraviolet emission in the Type Ia supernova LSQ12gdj: No evidence for ongoing shock interaction

R. A. Scalzo^{1,2*}, M. Childress^{1,2}, B. Tucker^{1,3}, F. Yuan^{1,2}, B. Schmidt^{1,2}, P. J. Brown⁴,
C. Contreras⁵, N. Morrell⁶, E. Hsiao⁶, C. Burns⁷, M. M. Phillips⁶, A. Campillay⁶,
C. Gonzalez⁶, K. Krisciunas⁴, M. Stritzinger⁵, M. L. Graham^{3,8}, J. Parrent^{8,9},
S. Valenti^{8,10}, C. Lidman¹¹, B. Schaefer¹², N. Scott¹³, M. Fraser^{14,15}, A. Gal-Yam¹⁶,
C. Inserra¹⁴, K. Maguire¹⁷, S. J. Smartt¹⁴, J. Sollerman¹⁸, M. Sullivan¹⁹, F. Taddia¹⁸,
O. Yaron¹⁶, D. R. Young¹⁴, S. Taubenberger²⁰, C. Baltay²¹, N. Ellman²¹, U. Feindt²²,
E. Hadjiyska²¹, R. McKinnon²¹, P. E. Nugent^{3,23}, D. Rabinowitz²¹, and E. S. Walker²¹

¹ Research School of Astronomy and Astrophysics, Australian National University, Canberra, ACT 2611, Australia

² ARC Centre of Excellence for All-Sky Astrophysics (CAASTRO)

³ Department of Astronomy, University of California, Berkeley, B-20 Hearst Field Annex #3411, Berkeley, CA 94720-3411, USA

⁴ George P. and Cynthia Woods Mitchell Institute for Fundamental Physics and Astronomy, Department of Physics and Astronomy, Texas A&M University, 4242 TAMU, College Station, TX 77843, USA

⁵ Department of Physics and Astronomy, Aarhus University, Ny Munkegade 120, DK-8000 Aarhus C, Denmark

⁶ Carnegie Observatories, Las Campanas Observatory, La Serena, Chile

⁷ Observatories of the Carnegie Institution for Science, Pasadena, CA 91101, USA

⁸ Las Cumbres Observatory Global Telescope Network, 6740 Cortona Dr., Suite 102, Goleta, CA 93117, USA

⁹ Department of Physics and Astronomy, Dartmouth College, Hanover, NH 03755, USA

¹⁰ Department of Physics, University of California, Santa Barbara, Broida Hall, Mail Code 9530, Santa Barbara, CA 93106-9530, USA

¹¹ Australian Astronomical Observatory, PO Box 296, Epping, NSW 1710, Australia

¹² Department of Physics and Astronomy, Louisiana State University, Baton Rouge, Louisiana 70803, USA

¹³ Center for Astrophysics & Supercomputing, Swinburne University of Technology, PO Box 218, Hawthorn, VIC 3122, Australia

¹⁴ Astrophysics Research Centre, School of Mathematics and Physics, Queen's University Belfast, Belfast, BT7 1NN, UK

¹⁵ Institute of Astronomy, University of Cambridge, Madingley Road, Cambridge, CB3 0HA, UK

¹⁶ Department of Particle Physics and Astrophysics, The Weizmann Institute of Science, Rehovot 76100, Israel

¹⁷ European Southern Observatory, Karl-Schwarzschild-Str. 2, 85748 Garching bei München, Germany

¹⁸ The Oskar Klein Centre, Department of Astronomy, Stockholm University, AlbaNova, 10691 Stockholm, Sweden

¹⁹ School of Physics and Astronomy, University of Southampton, Southampton, SO17 1BJ, UK

²⁰ Max-Planck-Institut für Astrophysik, Karl-Schwarzschild-Str. 1, 85741 Garching bei München, Germany

²¹ Department of Physics, Yale University, New Haven, CT 06520-8121, USA

²² Physikalisches Institut, Universität Bonn, Nussallee 12, 53115 Bonn, Germany

²³ Computational Cosmology Center, Computational Research Division, Lawrence Berkeley National Laboratory, 1 Cyclotron Road MS 50B-4206, Berkeley, CA 94720, USA

4 April 2014

ABSTRACT

We present photospheric-phase observations of LSQ12gdj, a slowly-declining, UV-bright Type Ia supernova. Classified well before maximum light, LSQ12gdj has extinction-corrected absolute magnitude $M_B = -19.8$, and pre-maximum spectroscopic evolution similar to SN 1991T and the super-Chandrasekhar-mass SN 2007if. We use ultraviolet photometry from *Swift*, ground-based optical photometry, and corrections from a near-infrared photometric template to construct the bolometric (1600–23800 Å) light curve out to 45 days past *B*-band maximum light. We estimate that LSQ12gdj produced $0.96 \pm 0.07 M_\odot$ of ^{56}Ni , with an ejected mass near or slightly above the Chandrasekhar mass. As much as 27% of the flux at the earliest observed phases, and 17% at maximum light, is emitted bluewards of 3300 Å. The absence of excess luminosity at late times, the cutoff of the spectral energy distribution bluewards of 3000 Å, and the absence of narrow line emission and strong Na I D absorption all argue against a significant contribution from ongoing shock interaction. However, up to 10% of LSQ12gdj's luminosity near maximum light could be produced by the release of trapped radiation, including kinetic energy thermalized during a brief interaction with a compact, hydrogen-poor envelope (radius $< 10^{13}$ cm) shortly after explosion; such an envelope arises generically in double-degenerate merger scenarios.

Key words: white dwarfs; supernovae: general; supernovae: individual (SN 2003fg, SN 2007if, SN 2009dc, LSQ12gdj)

1 INTRODUCTION

Type Ia supernovae (SNe Ia) have become indispensable as luminosity distance indicators at large distances appropriate for studying the cosmological dark energy (Riess et al. 1998; Perlmutter et al. 1999). They are believed to be the thermonuclear explosions of carbon-oxygen white dwarfs, and their spectra are generally very similar near maximum light, although some spectroscopic diversity exists (Branch et al. 1993; Benetti et al. 2005; Branch et al. 2006, 2007, 2008; Wang et al. 2009).

SNe Ia used for cosmology are referred to as spectroscopically “(Branch) normal” (Branch et al. 1993) SNe Ia; they have a typical absolute magnitude near maximum light in the range $-18.5 < M_V < -19.5$. They are used as robust standard candles based on empirical relations between the SN’s luminosity and its colour and light curve width (Riess et al. 1996; Tripp 1998; Phillips et al. 1999; Goldhaber et al. 2001). Maximum-light spectroscopic properties can also help to improve the precision of distances measured using normal SNe Ia (Bailey et al. 2009; Wang et al. 2009; Folatelli et al. 2010; Foley & Kasen 2011).

Another subclass of SNe Ia with absolute magnitude $M_V \sim -20$ has also attracted recent attention. At least three events are currently known: SN 2003fg (Howell et al. 2006), SN 2007if (Scalzo et al. 2010; Yuan et al. 2010), and SN 2009dc (Yamanaka et al. 2009; Tanaka et al. 2010; Silverman et al. 2011; Taubenberger et al. 2011). A fourth event, SN 2006gz (Hicken et al. 2007), is usually classed with these three, although its maximum-light luminosity depends on an uncertain extinction correction from dust in its host galaxy. These four events are spectroscopically very different from each other. Among the four events, SN 2006gz is the most spectroscopically normal near maximum light, with a photospheric velocity typical of normal SNe Ia as inferred from the velocity of the Si II $\lambda 6355$ absorption minimum, and C II absorption ($\lambda\lambda 4745, 6580, 7234$) in spectra taken more than 10 days before *B*-band maximum light. In contrast, SN 2009dc shows low Si II velocity v_{Si} ($\sim 8000 \text{ km s}^{-1}$), a relatively high Si II velocity gradient \dot{v}_{Si} ($\sim -75 \text{ km s}^{-1} \text{ day}^{-1}$), and very strong, persistent C II $\lambda 6580$ absorption. SN 2007if is spectroscopically 1991T-like before maximum light, its spectrum dominated by Fe III and showing only very weak Si II, with a definite C II detection in a spectrum taken 5 days after *B*-band maximum light. SN 2006gz, SN 2007if and SN 2009dc show low-ionization nebular spectra dominated by Fe II, in contrast to normal SNe Ia which have stronger Fe III emission (Maeda et al. 2009; Taubenberger et al. 2013). Only one spectrum, taken at 2 days past *B*-band maximum, exists for SN 2003fg, which resembles SN 2009dc at a similar phase. Recently two additional SNe, SN 2011aa and SN 2012dn, have been proposed as super-Chandrasekhar-mass SN Ia candidates based on their luminosity at ultraviolet (UV) wavelengths as observed with the *Swift* telescope (Brown et al. 2014).

These extremely luminous SNe Ia cannot presently be explained by models of exploding Chandrasekhar-mass white dwarfs, since these produce no more than $1 M_{\odot}$ of ^{56}Ni even in a pure detonation (Khokhlov et al. 1993). While they might more descriptively be called “superluminous SNe Ia”, these SNe Ia have typically been referred to as “candidate super-Chandrasekhar SNe Ia” or “super-Chandras”, based on an early interpretation of SN 2003fg as arising from the explosion of a differentially rotating white dwarf with mass $\sim 2 M_{\odot}$ (Howell et al. 2006). Observation of events in this class has stimulated much recent theoretical investigation into super-Chandrasekhar-mass SN Ia channels (Hachisu et al. 2011; Justham 2011; Di Stefano & Kilic 2012; Das & Mukhopadhyay

2013a,b), and into mechanisms for increasing the peak luminosity of Chandrasekhar-mass events (Hillebrandt et al. 2007).

The status of superluminous SNe Ia as being super-Chandrasekhar-mass has historically been closely tied to their peak luminosity. SN 2003fg’s ejected mass was inferred at first from its peak absolute magnitude $M_V = -19.94$, requiring a large mass of ^{56}Ni ($M_{\text{Ni}} = 1.3 \pm 0.1 M_{\odot}$; Arnett 1982) and a low Si II velocity near maximum ($\sim 8000 \text{ km s}^{-1}$), suggesting a high binding energy for the progenitor. Ejected mass estimates were later made for SN 2007if (Scalzo et al. 2010) and SN 2009dc (Silverman et al. 2011; Taubenberger et al. 2011), producing numbers of similar magnitude. These ejected mass estimates depend, to varying extents, on the interpretation of the maximum-light luminosity in terms of a large ^{56}Ni mass, which can be influenced by asymmetries and/or non-radioactive sources of luminosity. For example, shock interaction with a dense shroud of circumstellar material (CSM) has been proposed as a source of luminosity near maximum light for SN 2009dc (Taubenberger et al. 2011; Hachinger et al. 2012; Taubenberger et al. 2013). The CSM envelope would have to be largely free of hydrogen and helium to avoid producing emission lines of these elements in the shocked material. The additional luminosity could simply represent trapped radiation from a short interaction soon after explosion with a compact envelope, rather than an ongoing interaction with an extended wind. Such an envelope is naturally produced in an explosion resulting from a “slow” merger of two carbon-oxygen white dwarfs (Iben & Tutukov 1984; Shen et al. 2012). Khokhlov et al. (1993) modeled detonations of carbon-oxygen white dwarfs inside compact envelopes, calling them *tamped detonations*; these events are luminous and have long rise times, but appear much like normal SNe Ia after maximum light. A strong ongoing interaction with an extended wind, in contrast, is expected to produce very broad, ultraviolet (UV)-bright light curves and blue, featureless spectra uncharacteristic of normal SNe Ia (Fryer et al. 2010; Blinnikov & Sorokina 2010).

Searching for more candidate super-Chandrasekhar-mass SNe Ia, Scalzo et al. (2012) reconstructed masses for a sample of SNe Ia with spectroscopic behavior matching a classical 1991T-like template and showing very slow evolution of the Si II velocity, similar to SN 2007if; these events were interpreted as tamped detonations, and the mass reconstruction featured a very rough accounting for trapped radiation. One additional plausible super-Chandrasekhar-mass candidate event was found, SNF 20080723-012, with estimated ejected mass $\sim 1.7 M_{\odot}$ and ^{56}Ni mass $\sim 0.8 M_{\odot}$. The other events either had insufficient data to establish super-Chandrasekhar-mass status with high confidence, or had reconstructed masses consistent with the Chandrasekhar mass. However, none of the Scalzo et al. (2012) SNe had coverage at wavelengths bluer than 3300 \AA , making it impossible to search for early signatures of shock interaction, and potentially underestimating the maximum bolometric luminosity and the ^{56}Ni mass. While Brown et al. (2014) obtained good UV coverage of two new candidate super-Chandrasekhar-mass SNe Ia, 2011aa and 2012dn, no optical photometry redward of 6000 \AA has yet been published for these SNe, precluding the construction of their bolometric light curves or detailed inference of their masses.

In this paper we present observations of a new overluminous ($M_B = -19.8$) 1991T-like SN Ia, LSQ12gdj, including detailed UV (from *Swift*) and optical photometric coverage, as well as spectroscopic time series, starting at 10 days before *B*-band maximum light. We examine the UV behavior as a tracer of shock interaction and as a contribution to the total bolometric flux, in order to better understand the physical mechanisms behind the high luminosities of these events. Including the *Swift* UV filters and a correction for

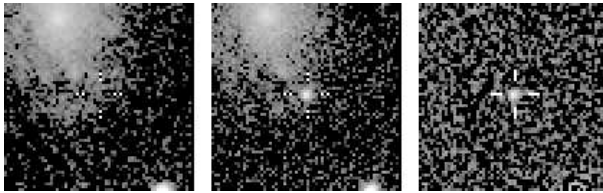


Figure 1. Discovery images for LSQ12gdj. Left: REF (galaxy template) image showing the host galaxy before the SN. Center: NEW image showing host galaxy + SN. Right: Subtraction SUB = NEW - REF, showing the SN alone. The thumbnails are $56'' \times 56''$ square.

unobserved near-infrared (NIR) flux, we construct the bolometric light curve of LSQ12gdj and use it to reconstruct the ^{56}Ni mass synthesized in the explosion and the total ejected mass.

2 OBSERVATIONS

2.1 Discovery and Classification

LSQ12gdj was discovered on 2012 Nov 07 UT as part of the La Silla-QUEST (LSQ) Low-Redshift Supernova Survey (Baltay et al. 2013), ongoing since 2009 using the QUEST-II camera mounted on the ESO 1-m Schmidt telescope at La Silla Observatory. QUEST-II observations are taken in a broad bandpass using a custom-made interference filter with appreciable transmission from 4000–7000 Å, covering the SDSS g' and r' bandpasses. Magnitudes were calibrated in the LSQ natural system against stars in the SN field with entries in the AAVSO All-Sky Photometric Survey (APASS) DR6 catalog. These images are processed regularly using an image subtraction pipeline, which uses reliable open-source software modules to subtract template images of the constant night sky, leaving variable objects. Each new image is registered and resampled to the position of a template image using SWARP (Bertin et al. 2002). The template image is then rescaled and convolved to match the point spread function (PSF) of the new image, before being subtracted from the new image using HOTPANTS¹. New objects on the subtracted images are detected using SExtractor (Bertin & Arnouts 1996). These candidates are then visually scanned and the most promising candidates selected for spectroscopic screening and follow-up.

The discovery image of LSQ12gdj, showing its position (RA = 23:54:43.32, DEC = $-25:40:34.0$) on the outskirts of its host galaxy, ESO 472- G 007 ($z = 0.030324$; Di Nella et al. 1996), is shown in Figure 1, along with the galaxy template image and the subtracted image. No source was detected at the SN position two days earlier (2012 Nov 05 UT) to a limiting magnitude of ~ 21 . Ongoing LSQ observations of LSQ12gdj were taken after discovery as part of the LSQ rolling search strategy, characterizing the rising part of the light curve.

The Nearby Supernova Factory (SNfactory) reported that a spectrum taken 2013 Nov 10.2 UT with the SuperNova Integral Field Spectrograph (SNIFS; Lantz et al. 2004) on the University of Hawaii 2.2-m telescope was a good match to a 1991T-like SN Ia before maximum light as classified using SNID (Blondin & Tonry 2007), and flagged it as a candidate super-Chandrasekhar-mass SN Ia (Cellier-Holzem et al. 2012). This classification was later confirmed by the first PESSTO spectrum in the time series described below, taken 2012 Nov 13 UT.

¹ <http://www.astro.washington.edu/users/becker/hotpants.html>

2.2 Photometry

Swift UVOT observations were triggered immediately after spectroscopic confirmation, providing comprehensive photometric coverage at UV wavelengths starting 8 days before B -band maximum light. The observations were reduced using aperture photometry according to the procedure in Brown et al. (2009), using the updated zeropoints, sensitivity corrections, and transmission curves of Breeveld et al. (2011).

Ground-based follow-up photometry was taken by the *Carnegie Supernova Project II* (CSP) using the Swope 1-m telescope at Las Campanas observatory, in the natural system CSP $BVr'i'$ filters, starting at 10 days before B -band maximum light. The SITe3 CCD detector mounted on the Swope has a 2048×4096 pix active area, with a pixel scale of 0.435 arcsec/pix; to reduce readout time, a 1200×1200 pix subraster is read out, for a field of view of 8.7×8.7 arcmin. The images were reduced with standard CSP software including bias subtraction, linearity correction, flat fielding and exposure correction. A local sequence of 20 stars around the SN, covering a wide range of magnitudes, has been calibrated on more than 15 photometric nights into the natural system of the Swope telescope, using the reduction procedures described in Contreras et al. (2010) and the bandpass calibration procedures and transmission functions in Stritzinger et al. (2012). Template images for galaxy subtractions were taken with the Du Pont 2.5-m telescope under favorable seeing conditions on the nights of 2013 Oct 10–11, using the same filter set as the science images. PSF-fitting photometry was performed on the SN detections in the template-subtracted images, relative to the local sequence stars, measured with the standard IRAF (Tody 1993) package DAOPHOT (Stetson 1987).

Additional ground-based photometry was taken by the Las Cumbres Global Telescope Network (LCOGT). The LCOGT data were reduced using a custom pipeline developed by the LCOGT SN team, using standard procedures (PYRAF, DAOPHOT, SWARP) in a PYTHON framework. PSF-fitting photometry is performed after subtraction of the background, estimated via a low-order polynomial fit.

The *Swift* UV photometry and the CSP/LCOGT optical photometry are shown in Tables 1 and 2, respectively, and plotted in Figure 6. All ground-based magnitudes have been S -corrected to the appropriate standard system Landolt (1992); Fukugita et al. (2010); the natural-system light curves are included separately.

2.3 Spectroscopy

A full spectroscopic time series was taken by the Public ESO Spectroscopic Survey for Transient Objects (PESSTO), using the EFOSC2 spectrograph on the ESO New Technology Telescope (NTT) at La Silla Observatory, comprising seven spectra taken between 2012 Nov 13 and 2013 Jan 13 UT. The $gr11$ and $gr16$ gratings were used, covering the entire wavelength range 3360–10330 Å at 13 Å resolution. The spectra were reduced using the PYRAF package as part of a custom-built, Python-based pipeline written for PESSTO; the pipeline includes corrections for bias and fringing, wavelength and flux calibration, correction for telluric absorption and a cross-check of the wavelength calibration using atmospheric emission lines.

Three spectra of LSQ12gdj were obtained around maximum light by CSP using the Las Campanas 2.5-m du Pont telescope and WFCCD. The spectral resolution is 8 Å, as measured from the FWHM of the HeNeAr comparison lines. A complete description of data reduction procedures can be found in Hamuy et al. (2006).

An additional five optical spectra were taken with the WiFeS integral field spectrograph on the ANU 2.3-m telescope at Siding Spring Observatory. WiFeS spectra were obtained using the B3000 and R3000 gratings, providing wavelength coverage in the range 3500–9600 Å with a FWHM resolution for the point-spread function (PSF) of 1.5 Å (blue channel) and 2.5 Å (red channel). Data cubes for WiFeS observations were produced using the PyWiFeS² software (Childress et al. 2013b). Spectra of the SN were extracted from final data cubes using a PSF-weighted extraction technique with a simple symmetric Gaussian PSF, and the width of this Gaussian was measured directly from the data cube. Background subtraction was performed by calculating the median background spectrum across all pixels outside a distance from the SN equal to about three times the seeing disk (typically 1''.5–2'' FWHM). Due to the negligible galaxy background and good spatial flat-fielding from the PyWiFeS pipeline, this technique produced favorable subtraction of the sky background from the WiFeS spectra of LSQ12gdj.

The observation log for all spectra presented is shown in Table 3. All spectra will be publicly available through WISEREP³ (Yaron & Gal-Yam 2012).

3 ANALYSIS

In this section we discuss quantities derived from the photometry and spectroscopy in more detail. We characterize the spectroscopic evolution of LSQ12gdj, including the velocities of common absorption features, in §3.1. We discuss the broad-band light curves of LSQ12gdj and estimate the host galaxy extinction in §3.2. Finally, we describe the construction of a bolometric light curve for LSQ12gdj in §3.3, including correction for unobserved NIR flux and the process of solving for a low-resolution broad-band spectral energy distribution (SED).

3.1 Spectral Features and Velocity Evolution

Figure 2 shows the spectroscopic evolution of LSQ12gdj, with spectra of the super-Chandrasekhar-mass SN 2007if included for comparison. The early spectra show evidence for a hot photosphere, with a blue continuum and absorption features dominated by Fe II and Fe III, typical of 1991T-like SNe Ia Filippenko et al. (1992); Phillips et al. (1992). These include absorption complexes near 3500 Å, attributed to iron-peak elements (Ni II, Co II, and Cr II) in SN 2007if (Scalzo et al. 2010). The prominence of hot iron-peak elements in the outer layers is consistent with a great deal of ⁵⁶Ni being produced, and/or with significant mixing of ⁵⁶Ni throughout the outer layers of ejecta during the explosion. Si II λ5972 is not visible. Si II λ6355 and Ca II H+K are weak throughout the evolution.

Figure 3 shows subranges of the spectra highlighting common intermediate-mass element lines at key points in their evolution. LSQ12gdj shows unusually narrow intermediate-mass-element signatures. The Ca II H+K absorption is narrow enough (~6000 kms FWHM) that the minimum is unblended with neighboring Si II λ3858, and both components of the doublet can be seen in the line profile (though still blended) at ~10000 km s⁻¹. At later phases, the separate components of the Ca II NIR triplet can also be seen at 12000 km s⁻¹. Spectra at the earliest phases show absorption minima near the expected positions of all of these lines

near maximum light, but with unexpected shapes; these lines may not correspond physically to the nearest familiar feature in each case, but if they do, they may yield interesting information about the level populations to detailed modelling which properly accounts for the ionization balance. An example of such ambiguity is the feature near 3650 Å in the pre-maximum spectra, the position of which is consistent with high-velocity Ca II as in normal SNe Ia, but is also near the expected position of Si III around 12000 km s⁻¹.

To identify various line features in a more comprehensive manner, we fit the maximum-light spectrum of LSQ12gdj using SYN++ (Thomas et al. 2011), shown in Figure 4. While LSQ12gdj displays many features typical of SNe Ia near maximum light, our fit also suggests contributions from higher ionization species, e.g., C III λ4649 over Fe II/S II absorption complexes, or Si III near 3650 Å and 4400 Å in the pre-maximum spectra. These identifications, though tentative (labelled in red in Figure 4), are consistent with spectroscopic behaviors seen in shallow-silicon events prior to maximum light (Branch et al. 2006). The suggestion of C III λ4649 near 18,000 km s⁻¹ is tantalizing, but ambiguous, and no corresponding C II λ6580 absorption is evident. Cr II is an intriguing possibility, since it provides a better fit in the bluest part of the spectrum and simultaneously contributes strong line blanketing in the unobserved UV part of the spectrum; such line blanketing is in line with the sharp cutoff of our photometry-based SED in the *Swift* bands (see §3.3). However, given the degeneracies involved in identifying highly blended species, we do not consider Cr II to have been definitively detected in LSQ12gdj.

We measure the absorption minimum velocities of common lines in a less model-dependent way using a method similar to Scalzo et al. (2012). We resample each spectrum to log(λ), i.e., to velocity space, then smooth it with wide (“continuum”; ~75000 km s⁻¹) and narrow (“lines”; ~3500 km s⁻¹) third-order Savitzsky-Golay filters, which retain detail in the intrinsic line shapes more effectively than rebinning or conventional Gaussian filtering. After dividing out the continuum to produce a smoothed spectrum with only line features, we measure the absorption minima and estimate the statistical errors by Monte Carlo sampling. We track the full covariance matrix of the spectrum from the original reduced data to the final smoothed version, and use its Cholesky decomposition to produce Monte Carlo realizations. We add in quadrature a systematic error equal to the RMS spectrograph resolution, which may affect the observed line minimum since we are not assuming a functional form (e.g. a Gaussian) for the line profile. The resulting velocities are shown in Figure 5. In calculating velocities from wavelengths, we assume nearby component multiplets are blended, with the rest wavelength of each line being the *g*-weighted rest wavelengths of the multiplet components, although this approximation may break down for some lines (see Figure 3).

LSQ12gdj shows slow velocity evolution in the absorption minima of intermediate mass elements, again characteristic of SN 1991T (Phillips et al. 1992) and other candidate super-Chandrasekhar-mass events with 1991T-like spectra (Scalzo et al. 2010, 2012). At early times, familiar absorption features of intermediate-mass elements are either ambiguously identified or too weak for their properties to be measured reliably, but come clearly into focus by maximum light. Before maximum, the measured velocities for Si II λ3858 differ by as much as 1000 km s⁻¹ between neighboring WiFeS and CSP spectra. The most likely source of the discrepancy is systematic error in the continuum estimation for this shallow line near the blue edge of each spectrograph’s sensitivity, since the relative prominence of the local maxima on either side of the line differ between CSP and WiFeS. For other line minima, measurements from CSP and from WiFeS are

² <http://www.mso.anu.edu.au/pywifes/doku.php>

³ <http://www.weizmann.ac.il/astrophysics/wiserep/>

Table 1. Swift photometry of LSQ12gdj

MJD	Phase ^a	<i>uvw2</i>	<i>uvm2</i>	<i>uvw1</i>	<i>u</i>	<i>b</i>	<i>v</i>
56243.9	-8.4	18.34 ± 0.11	18.63 ± 0.11	16.56 ± 0.08	15.41 ± 0.05	16.65 ± 0.07	16.77 ± 0.09
56246.2	-6.1	18.07 ± 0.10	18.57 ± 0.11	16.34 ± 0.08	15.16 ± 0.04	16.25 ± 0.06	16.34 ± 0.08
56249.2	-3.2	18.07 ± 0.10	18.42 ± 0.10	16.40 ± 0.08	15.02 ± 0.04	16.02 ± 0.05	16.21 ± 0.08
56252.1	-0.4	18.21 ± 0.11	18.49 ± 0.10	16.61 ± 0.08	15.08 ± 0.04	15.98 ± 0.05	16.15 ± 0.07
56255.2	2.6	18.42 ± 0.11	18.69 ± 0.11	16.98 ± 0.08	15.36 ± 0.05	16.00 ± 0.05	16.12 ± 0.07
56258.7	6.0	18.68 ± 0.12	18.85 ± 0.12	17.43 ± 0.09	15.67 ± 0.06	16.08 ± 0.05	16.07 ± 0.07
56261.1	8.4	18.89 ± 0.13	19.32 ± 0.15	17.78 ± 0.09	15.96 ± 0.07	16.17 ± 0.05	16.14 ± 0.07
56264.3	11.4	19.54 ± 0.18	19.51 ± 0.17	18.09 ± 0.10	16.39 ± 0.08	16.42 ± 0.06	16.27 ± 0.08
56267.3	14.3	19.82 ± 0.21	20.10 ± 0.25	18.59 ± 0.13	16.88 ± 0.09	16.73 ± 0.08	16.42 ± 0.08
56270.8	17.7	20.08 ± 0.25	20.48 ± 0.32	18.93 ± 0.16	17.38 ± 0.10	17.18 ± 0.08	16.66 ± 0.09
56279.4	26.1	19.61 ± 0.26	18.40 ± 0.17	18.18 ± 0.12	17.11 ± 0.10
56286.3	32.8	19.02 ± 0.25	18.76 ± 0.17	17.49 ± 0.13
56293.4	39.7	19.91 ± 0.33	18.98 ± 0.28	19.11 ± 0.24	17.71 ± 0.16
56300.1	46.2	19.17 ± 0.25	18.13 ± 0.22

^a Phase given in rest-frame days since *B*-band maximum light.

Table 2. Ground-based photometry of LSQ12gdj in the Landolt and SDSS standard systems

MJD	Phase ^a	<i>B</i>	<i>V</i>	<i>g</i>	<i>r</i>	<i>i</i>	<i>z</i>	Source
56242.1	-10.2	17.02 ± 0.01	17.05 ± 0.01	...	17.19 ± 0.01	17.47 ± 0.01	...	SWOPE
56243.1	-9.2	16.76 ± 0.01	16.81 ± 0.01	...	16.94 ± 0.01	17.20 ± 0.01	...	SWOPE
56245.0	-7.3	16.38 ± 0.01	16.52 ± 0.01	16.81 ± 0.02	17.28 ± 0.01	LCOGT
56245.1	-7.2	16.40 ± 0.01	16.46 ± 0.01	...	16.57 ± 0.01	16.84 ± 0.01	...	SWOPE
56246.0	-6.3	16.29 ± 0.01	16.34 ± 0.01	...	16.46 ± 0.01	16.74 ± 0.01	...	SWOPE
56246.0	-6.3	16.30 ± 0.01	16.45 ± 0.02	16.72 ± 0.01	17.05 ± 0.02	LCOGT
56247.0	-5.3	16.17 ± 0.01	16.31 ± 0.02	16.65 ± 0.01	16.95 ± 0.02	LCOGT
56247.1	-5.3	16.18 ± 0.01	16.24 ± 0.01	...	16.35 ± 0.01	16.67 ± 0.01	...	SWOPE
56248.1	-4.3	16.11 ± 0.01	16.16 ± 0.01	...	16.26 ± 0.00	16.62 ± 0.01	...	SWOPE
56248.1	-4.3	16.11 ± 0.01	16.29 ± 0.01	16.62 ± 0.02	16.86 ± 0.02	LCOGT
56249.0	-3.4	16.04 ± 0.01	16.09 ± 0.01	...	16.19 ± 0.00	16.59 ± 0.01	...	SWOPE
56250.0	-2.4	15.99 ± 0.01	16.04 ± 0.01	...	16.12 ± 0.01	16.58 ± 0.01	...	SWOPE
56250.1	-2.3	15.98 ± 0.01	16.14 ± 0.02	16.58 ± 0.01	16.71 ± 0.02	LCOGT
56251.0	-1.4	15.97 ± 0.01	16.02 ± 0.01	...	16.06 ± 0.01	16.55 ± 0.01	...	SWOPE
56252.0	-0.5	15.97 ± 0.01	16.00 ± 0.01	...	16.03 ± 0.01	16.57 ± 0.01	...	SWOPE
56252.1	-0.4	15.93 ± 0.01	16.04 ± 0.01	16.59 ± 0.01	16.71 ± 0.01	LCOGT
56253.0	0.5	15.98 ± 0.01	15.98 ± 0.01	...	16.00 ± 0.00	16.58 ± 0.01	...	SWOPE
56253.1	0.6	15.92 ± 0.01	16.03 ± 0.01	16.61 ± 0.01	16.68 ± 0.01	LCOGT
56254.1	1.5	15.99 ± 0.01	15.96 ± 0.01	...	15.96 ± 0.01	16.60 ± 0.01	...	SWOPE
56254.1	1.6	15.90 ± 0.01	16.02 ± 0.01	16.58 ± 0.02	16.64 ± 0.01	LCOGT
56255.1	2.5	15.99 ± 0.01	15.96 ± 0.01	...	15.95 ± 0.01	16.60 ± 0.01	...	SWOPE
56255.1	2.5	15.93 ± 0.01	15.97 ± 0.01	16.62 ± 0.01	16.69 ± 0.02	LCOGT
56256.1	3.4	16.05 ± 0.02	15.96 ± 0.01	...	15.94 ± 0.01	16.62 ± 0.01	...	SWOPE
56256.1	3.5	15.90 ± 0.01	15.97 ± 0.01	16.55 ± 0.02	16.72 ± 0.02	LCOGT
56257.1	4.4	16.03 ± 0.01	15.95 ± 0.01	...	15.92 ± 0.01	16.63 ± 0.01	...	SWOPE
56257.1	4.5	15.94 ± 0.01	15.96 ± 0.01	16.62 ± 0.02	16.76 ± 0.02	LCOGT
56258.1	5.4	16.07 ± 0.01	15.95 ± 0.01	...	15.95 ± 0.01	16.65 ± 0.01	...	SWOPE
56258.1	5.5	16.00 ± 0.01	15.94 ± 0.01	16.65 ± 0.01	16.80 ± 0.02	LCOGT
56259.0	6.3	16.10 ± 0.01	15.96 ± 0.01	...	15.96 ± 0.01	16.68 ± 0.01	...	SWOPE
56259.1	6.4	16.03 ± 0.01	15.94 ± 0.01	16.69 ± 0.03	16.83 ± 0.02	LCOGT
56261.1	8.3	16.20 ± 0.01	16.01 ± 0.01	...	16.03 ± 0.01	16.79 ± 0.01	...	SWOPE
56261.1	8.4	16.09 ± 0.01	16.09 ± 0.01	16.85 ± 0.01	17.01 ± 0.01	LCOGT
56262.1	9.3	16.25 ± 0.01	16.04 ± 0.01	...	16.09 ± 0.01	16.90 ± 0.01	...	SWOPE
56263.1	10.2	16.30 ± 0.01	16.10 ± 0.01	...	16.16 ± 0.01	16.99 ± 0.01	...	SWOPE
56264.1	11.2	16.39 ± 0.01	16.16 ± 0.01	17.09 ± 0.01	...	SWOPE
56264.1	11.3	16.21 ± 0.01	16.21 ± 0.03	17.06 ± 0.00	17.10 ± 0.02	LCOGT

^a Phase given in rest-frame days since *B*-band maximum light.

Table 2. Ground-based photometry of LSQ12gdj, cont'd.

MJD	Phase ^a	<i>B</i>	<i>V</i>	<i>g</i>	<i>r</i>	<i>i</i>	<i>z</i>	Source
56265.1	12.2	16.48 ± 0.01	16.24 ± 0.01	...	16.31 ± 0.01	17.18 ± 0.01	...	SWOPE
56265.1	12.2	16.31 ± 0.01	16.31 ± 0.01	17.17 ± 0.01	17.11 ± 0.01	LCOGT
56266.1	13.1	16.56 ± 0.01	16.29 ± 0.01	...	16.39 ± 0.01	17.28 ± 0.01	...	SWOPE
56266.1	13.2	16.38 ± 0.01	16.39 ± 0.01	17.24 ± 0.03	17.15 ± 0.02	LCOGT
56267.1	14.1	16.68 ± 0.01	16.36 ± 0.01	...	16.46 ± 0.01	17.32 ± 0.01	...	SWOPE
56267.1	14.2	16.48 ± 0.01	16.48 ± 0.01	17.32 ± 0.01	17.21 ± 0.02	LCOGT
56268.1	15.1	16.79 ± 0.01	16.43 ± 0.01	...	16.52 ± 0.01	17.37 ± 0.01	...	SWOPE
56268.1	15.1	16.58 ± 0.01	16.50 ± 0.01	17.35 ± 0.01	17.22 ± 0.02	LCOGT
56269.1	16.1	16.65 ± 0.01	16.55 ± 0.01	17.33 ± 0.01	17.18 ± 0.02	LCOGT
56270.1	17.0	16.75 ± 0.01	16.55 ± 0.01	17.30 ± 0.02	17.18 ± 0.02	LCOGT
56270.1	17.0	17.03 ± 0.01	16.56 ± 0.01	...	16.58 ± 0.01	17.36 ± 0.01	...	SWOPE
56272.1	19.0	16.95 ± 0.01	16.63 ± 0.02	17.29 ± 0.03	17.20 ± 0.02	LCOGT
56273.1	20.0	17.02 ± 0.01	16.63 ± 0.01	17.27 ± 0.01	17.17 ± 0.01	LCOGT
56274.1	20.9	17.03 ± 0.01	16.65 ± 0.01	17.19 ± 0.01	17.20 ± 0.02	LCOGT
56275.1	21.9	17.60 ± 0.01	16.85 ± 0.01	...	16.69 ± 0.01	17.23 ± 0.01	...	SWOPE
56275.1	21.9	17.17 ± 0.01	16.65 ± 0.02	17.20 ± 0.01	17.12 ± 0.01	LCOGT
56276.1	22.9	17.34 ± 0.01	16.69 ± 0.01	17.22 ± 0.01	17.17 ± 0.01	LCOGT
56277.1	23.8	17.40 ± 0.01	16.71 ± 0.03	17.18 ± 0.01	17.17 ± 0.02	LCOGT
56278.1	24.8	17.50 ± 0.01	16.76 ± 0.01	17.17 ± 0.03	17.17 ± 0.01	LCOGT
56279.1	25.8	17.52 ± 0.01	16.79 ± 0.01	17.19 ± 0.01	17.20 ± 0.02	LCOGT
56282.1	28.7	17.81 ± 0.01	16.87 ± 0.02	17.18 ± 0.01	17.21 ± 0.14	LCOGT
56283.1	29.7	17.89 ± 0.01	16.92 ± 0.01	17.22 ± 0.01	17.24 ± 0.03	LCOGT
56283.1	29.7	18.36 ± 0.02	17.24 ± 0.01	...	16.93 ± 0.01	17.23 ± 0.01	...	SWOPE
56284.0	30.6	18.42 ± 0.02	17.31 ± 0.02	...	16.96 ± 0.01	17.26 ± 0.01	...	SWOPE
56284.1	30.6	17.86 ± 0.02	16.97 ± 0.01	17.15 ± 0.01	17.28 ± 0.02	LCOGT
56285.0	31.6	18.44 ± 0.02	17.31 ± 0.01	...	17.01 ± 0.01	17.26 ± 0.01	...	SWOPE
56285.1	31.6	18.03 ± 0.01	16.96 ± 0.01	17.23 ± 0.01	17.37 ± 0.02	LCOGT
56286.1	32.6	18.02 ± 0.01	17.05 ± 0.01	17.26 ± 0.01	17.34 ± 0.02	LCOGT
56287.1	33.5	18.06 ± 0.01	17.02 ± 0.02	17.37 ± 0.02	17.32 ± 0.01	LCOGT
56288.0	34.5	18.59 ± 0.02	17.43 ± 0.01	...	17.12 ± 0.01	17.37 ± 0.01	...	SWOPE
56288.1	34.5	18.17 ± 0.01	17.10 ± 0.01	17.38 ± 0.01	17.44 ± 0.02	LCOGT
56289.1	35.5	18.18 ± 0.02	17.10 ± 0.02	17.45 ± 0.03	17.41 ± 0.02	LCOGT
56290.1	36.4	18.25 ± 0.02	17.18 ± 0.01	17.46 ± 0.01	17.52 ± 0.03	LCOGT
56291.1	37.4	18.33 ± 0.01	17.27 ± 0.01	17.49 ± 0.01	17.61 ± 0.02	LCOGT
56292.0	38.4	...	17.62 ± 0.02	...	17.29 ± 0.01	17.54 ± 0.01	...	SWOPE
56294.0	40.3	...	17.77 ± 0.02	...	17.40 ± 0.01	17.68 ± 0.01	...	SWOPE
56296.1	42.2	...	17.84 ± 0.02	...	17.49 ± 0.01	17.77 ± 0.01	...	SWOPE
56297.1	43.2	...	17.89 ± 0.02	...	17.55 ± 0.01	17.83 ± 0.01	...	SWOPE
56299.1	45.2	...	17.98 ± 0.02	...	17.64 ± 0.01	17.95 ± 0.01	...	SWOPE
56316.0	61.6	...	18.48 ± 0.04	...	18.31 ± 0.03	18.77 ± 0.04	...	SWOPE
56318.0	63.6	...	18.55 ± 0.03	SWOPE

^a Phase given in rest-frame days since *B*-band maximum light.

consistent with each other within the errors. For both Si II $\lambda 3858$ and Si II $\lambda 6355$, $\dot{v}_{\text{Si}} < 10 \text{ km s}^{-1}$ from maximum light until those lines become fully blended with developing Fe II lines more than three weeks past *B*-band maximum. The Si II plateau velocity is higher ($\sim 11000 \text{ km s}^{-1}$) than any of the Scalzo et al. (2012) SNe. The velocity of Ca II H+K seems to decrease by about 500 km s^{-1} between day +7 and day +14, but on the whole it remains steady near 10000 km s^{-1} , with a velocity gradient consistent with that of Si II. The S II $\lambda \lambda 5454, 5640$ “W” feature, which often appears at lower velocities than Si II, also appears around 11000 km s^{-1} until blending with developing Fe II features erases it.

These velocity plateaus may be a sign of a density enhancement in the outer ejecta, characteristic of a disturbed density structure resulting from an interaction with overlying material at early times (Scalzo et al. 2012), as in the DET2ENV2, DET2ENV4, and DET2ENV6 “tamped detonation” scenarios of Höflich & Khokhlov (1996), hereafter collectively called “DET2ENVN”. Alternatively, the plateau may simply mark

the outer edge of the iron-peak element core of the ejecta, as proposed in the case of the relatively normal SN Ia 2012fr (Childress et al. 2013a), which also featured extremely narrow (FWHM $< 3000 \text{ km s}^{-1}$) absorption features. SN 2012fr showed prominent high-velocity Si II absorption features, making it incompatible with a tamped detonation explosion scenario, since any SN ejecta above the shock velocity would have been swept into the reverse-shock shell. No signs of high-velocity absorption features from Ca, Si, or S are clearly evident in LSQ12gdj, although we might expect such material to be difficult to detect in shallow-silicon events like LSQ12gdj (Branch et al. 2006).

3.2 Maximum-Light Behavior, Colors, and Extinction

The reddening due to Galactic dust extinction towards the host of LSQ12gdj is $E(B - V)_{\text{MW}} = 0.021 \text{ mag}$ (Schlafly & Finkbeiner 2011). LSQ12gdj was discovered on the outskirts of a spiral galaxy viewed face-on, so we expect minimal extinction by dust in the

Table 3. Optical spectroscopy of LSQ12gdj

UT Date	MJD	Phase ^a (days)	Telescope / Instrument	Exposure Time (s)	Wavelength Range (Å)	Observers ^b
2012 Nov 13.13	56244.1	-8.1	NTT-3.6m / EFOSC	1500	3360–10000	PESSTO
2012 Nov 15.14	56246.1	-6.2	NTT-3.6m / EFOSC	1500	3360–10000	PESSTO
2012 Nov 17.43	56248.4	-4.0	ANU-2.3m / WiFeS	1200	3500–9550	NS
2012 Nov 19.52	56250.5	-1.9	ANU-2.3m / WiFeS	1200	3500–9550	MC
2012 Nov 19.92	56250.9	-1.6	DuPont / WFCCD	2 × 600	3580–9620	NM
2012 Nov 20.43	56251.4	-1.1	ANU-2.3m / WiFeS	1200	3500–9550	MC
2012 Nov 20.93	56251.9	-0.6	DuPont / WFCCD	2 × 600	3580–9620	NM
2012 Nov 21.45	56252.5	-0.1	ANU-2.3m / WiFeS	1200	3500–9550	MC
2012 Nov 21.85	56252.9	+0.3	DuPont / WFCCD	2 × 600	3580–9620	NM
2012 Nov 23.15	56254.1	+1.6	NTT-3.6m / EFOSC	900	3360–10000	PESSTO
2012 Nov 29.47	56260.5	+7.7	ANU-2.3m / WiFeS	1200	3500–9550	CL,BS
2012 Dec 06.12	56267.1	+14.2	NTT-3.6m / EFOSC	1500	3360–10000	PESSTO
2012 Dec 14.13	56275.1	+21.9	NTT-3.6m / EFOSC	1500	3360–10000	PESSTO
2012 Dec 23.13	56284.1	+30.7	NTT-3.6m / EFOSC	900	3360–10000	PESSTO
2013 Jan 13.05	56305.1	+51.0	NTT-3.6m / EFOSC	2 × 1500	3360–10000	PESSTO

^a In rest-frame days with respect to B-band maximum (MJD 56252.4).

^b BS = Brad Schaefer, CL = Chris Lidman, MC = Mike Childress, NM = Nidia Morrell, NS = Nicholas Scott

host galaxy. The equivalent width of Na I D absorption is 0.05 ± 0.03 Å Maguire et al. (2013), also consistent with little to no host galaxy extinction. A fit to the Folatelli et al. (2010) version of the Lira relation (Phillips et al. 1999) to the CSP B and V light curves suggests $E(B - V)_{\text{host}} = 0.02 \pm 0.08$ mag, consistent with zero.

To obtain more precise quantitative constraints for use in later modeling, we apply a multi-band light curve Bayesian analysis method to the CSP light curve of LSQ12gdj, trained on normal SNe Ia with a range of decline rates (Burns et al., in prep). This method provides joint constraints on $E(B - V)_{\text{host}}$ and the slope $R_{V,\text{host}}$ of a Cardelli et al. (1988) dust law. We find $E(B - V)_{\text{host}} = 0.013 \pm 0.005$ mag and $R_V = 1.66 \pm 1.66$ (a truncated Gaussian with $0 < R_V < 10$), with covariance $C(E(B - V)_{\text{host}}, R_{V,\text{host}}) = -0.0039$ mag. We adopt these values for our analysis.

As in Scalzo et al. (2014), we perform Gaussian process (GP) regression on the light curve of each individual band, using the Python module SKLEARN (Pedregosa et al. 2011), as a convenient form of interpolation for missing data. Gaussian process regression is a machine learning technique which can be used to fit generic smooth curves to data without assuming a particular functional form; we refer the reader to Rasmussen & Williams (2006) for more details. Neighboring points on the GP fit are covariant; we use a squared-exponential covariance function $k(t, t') = e^{-(t-t')^2/2\tau^2}$, with $0.5 < \tau < 2.0$. When performing the fit, we include an extra term $\sigma_i^2 \delta(t - t_i)$ describing the statistical noise on the observations at times t_i with errors σ_i ; we neglect this noise term when predicting values from the fit.

Figure 6 shows the light curve of LSQ12gdj in all available bands, S -corrected to the appropriate standard system: LSQ; Swift UVOT $uvw1$, $uvm2$, $uvw2$, and ubv ; Landolt BV ; and SDSS $griz$. Using the CSP bands, the SIFTO light curve fitter (Conley et al. 2008) gives a light curve stretch $s = 1.13 \pm 0.01$ and MJD of B -band maximum 56253.4. The SALT2.2 light curve fitter (Guy et al. 2007, 2010) gives consistent results ($x_1 = 0.96 \pm 0.05$, $c = -0.048 \pm 0.026$), though with a slightly later date for B -band maximum (MJD = 56253.8). Using one-dimensional GP regression fits to each separate band yields B -band maximum at MJD 56252.5 (2012 Nov 21.5, which we adopt henceforth), colour at B -band maximum $(B - V)_{\text{max}} = -0.019 \pm 0.005$, $\Delta m_{15}(B) = 0.74 \pm 0.01$, and peak magnitudes $m_B = 15.972 \pm 0.004$, $m_V =$

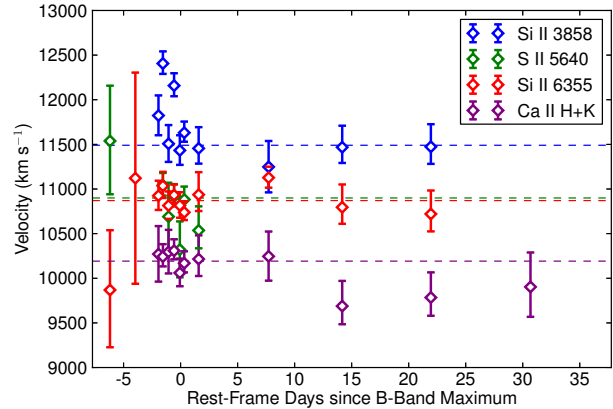


Figure 5. Blueshift velocities of absorption minima of intermediate-mass element lines in the LSQ12gdj spectral time series. Horizontal dashed lines indicate the median velocity. Asymmetric error bars represent the 68% CL region for the absorption line minimum.

15.947 ± 0.004 . These errors are statistical only; systematic errors are probably around 2%. After correction for the mean expected reddening, we derive peak absolute magnitudes $M_B = -19.78$, $M_V = -19.77$, using a distance modulus $\mu = 35.60 \pm 0.07$ derived from the redshift assuming a Λ CDM cosmology with $H_0 = 67.3$ km s⁻¹ Mpc⁻¹ (Ade et al. 2013) and a random peculiar velocity of 300 km s⁻¹.

We find a fairly substantial (~ 0.2 mag) mismatch between *Swift* b and CSP B , and between *Swift* v and CSP V , near maximum light; at later times, *Swift* and CSP observations agree within the errors (of the *Swift* points). The shape of the light curve is strongly constrained by CSP data, so we use CSP data in constructing the bolometric light curve at a given phase when both *Swift* and CSP observations are available.

The second maximum in the CSP i light curve appears earlier (+25 days) than expected for LSQ12gdj's $\Delta m_{15}(B)$ (+30 days Folatelli et al. 2010). The contrast of the second maximum is also fairly low, with a difference of -0.63 mag with the first maximum and $+0.20$ mag with the preceding minimum. Similar behavior is

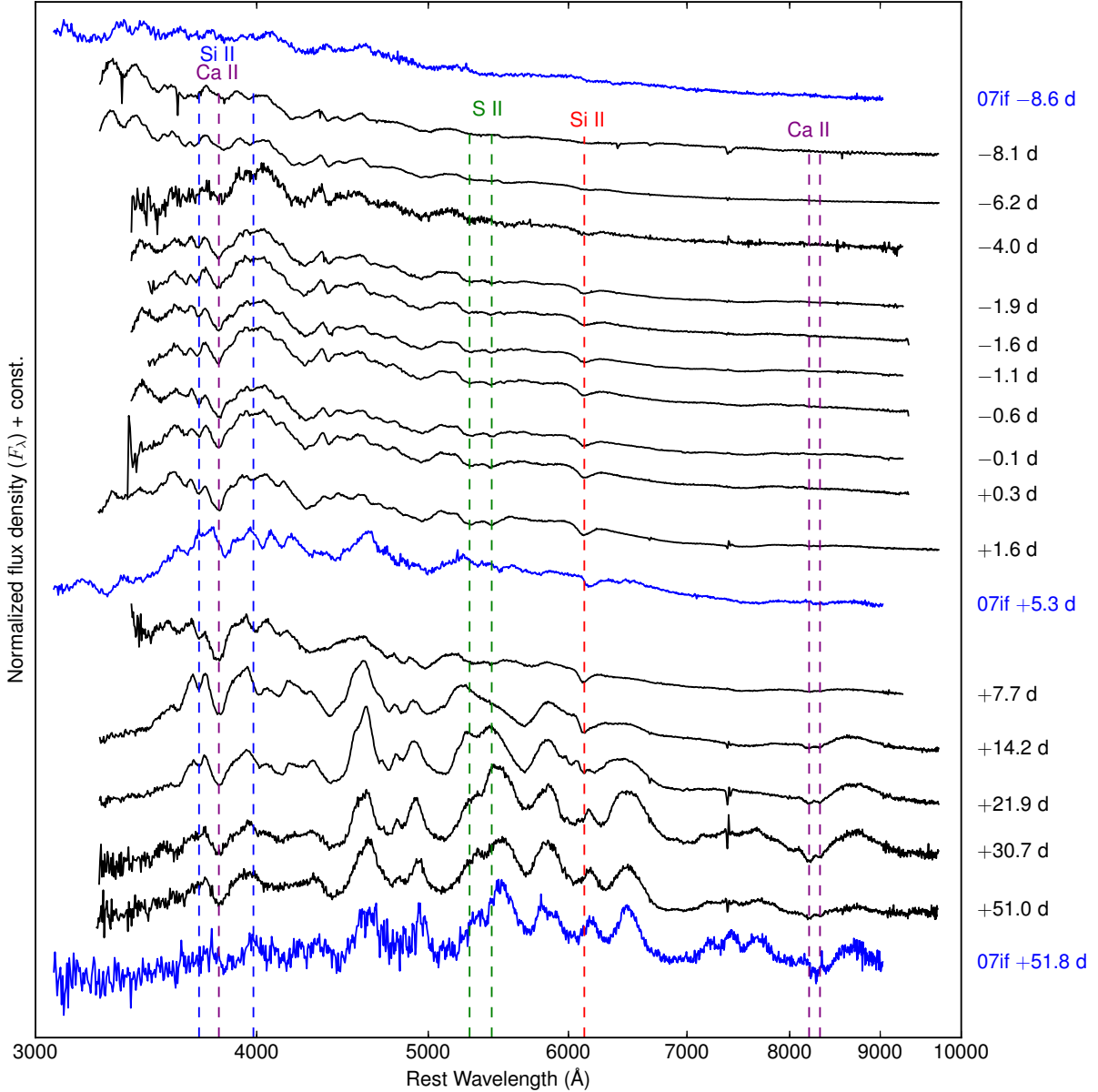


Figure 2. Spectral time series of LSQ12gdj (black solid lines, phase labels on right), shown with spectra of SN 2007if (blue solid lines, rest-frame phase labels on right; Scalzo et al. 2012) for comparison. All spectra have been rebinned to 5 Å. Constant velocity locations for absorption minima of various intermediate-mass element absorption features are marked with dashed lines: purple, Ca II H+K and NIR (10000 km s^{-1}); blue, Si II $\lambda\lambda 3858, 4129$ (11500 km s^{-1}); red, Si II $\lambda\lambda 6355$ (11000 km s^{-1}); green, S II $\lambda\lambda 5454, 5640$ (10500 km s^{-1}).

seen in LCOGT z . These properties are typical of low- ^{56}Ni explosions among the Chandrasekhar-mass models of Kasen (2006), difficult to reconcile with LSQ12gdj’s high luminosity. The low contrast persists even when CSP i and LCOGT z are S -corrected to Landolt I for more direct comparison with Kasen (2006). If LSQ12gdj synthesized a high mass of ^{56}Ni , comparison with the models of Kasen (2006) suggests that LSQ12gdj has substantial mixing of ^{56}Ni into its outer layers (as we might expect from its spectrum), a high yield of stable iron-peak elements, or both.

Fitting a $t^{2.0 \pm 0.2}$ rise to the first four points of the LSQ light curve suggests an explosion date of MJD 56236.2, giving a B -band

rise time of 16.3 ± 0.3 days. The pre-explosion upper limit is compatible with a t^2 rise, but does not permit LSQ12gdj to be visible much before B -band phase -16 . As pointed out by Piro & Nakar (2013, 2014), the t^2 functional form is at best approximate and does not take the distribution of ^{56}Ni in the outer layers properly into account; the explosion could in principle have had a “dark phase” before the onset of normal emission. Nevertheless, LSQ12gdj has a significantly shorter visible rise than other SNe Ia with similar decline rates (Ganeshalingam et al. 2011), and much shorter than the 24-day visible rise of SN 2007if (Scalzo et al. 2010) determined by the same method.

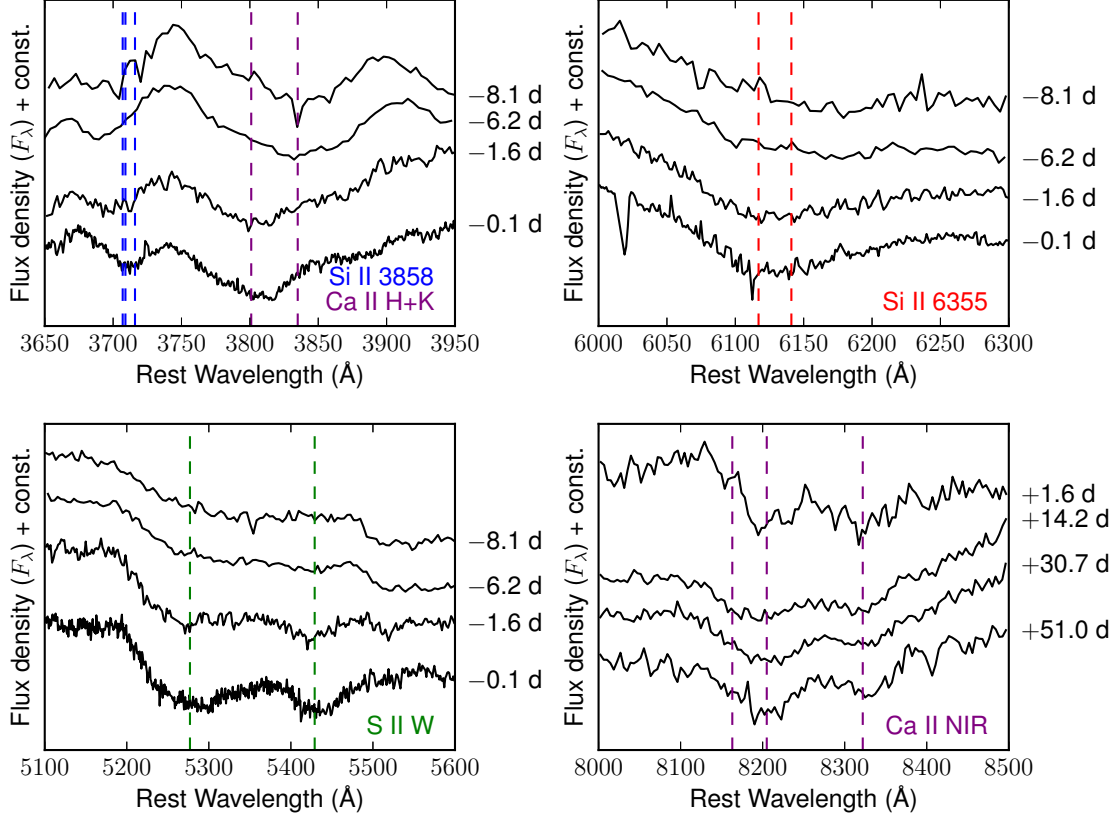


Figure 3. Subranges of spectra showing absorption line profiles of intermediate-mass elements in the LSQ12gdj spectral time series. Vertical dashed lines indicate the velocity of every component of each absorbing multiplet near maximum light. Phases shown along the right-hand edges of the plots are in rest-frame days with respect to B -band maximum light, as in Figure 2.

3.3 Bolometric Light Curve

We construct a bolometric light curve for LSQ12gdj in the rest-frame wavelength range 1550–23100 Å using the available photometry, as follows.

We first generate quasi-simultaneous measurements of all bandpasses at each epoch in Tables 2 and 1. We interpolate the values of missing measurements at each using the GP fits shown in Figure 6. After observations from a given band cease because the SN is no longer detected against the background, we estimate upper limits on the flux by assuming that the mean colours of the SN do not change since the last available observation — in particular that the SN does not become bluer in the *Swift* bands. If the last measurement in band j was taken at time $t_{\text{last},j}$, then at all future times t_i we form the predictions

$$m_{i,j,j'} = m_{i,j'} + (m_{\text{last},j} - m_{\text{last},j'}) \quad (1)$$

and set the upper limit $m_{i,j}$ by averaging $m_{i,j,j'}$ over all remaining bands j' . We estimate, and propagate, a systematic error on this procedure by taking the standard deviation of $m_{i,j,j'}$ over all remaining bands j' . All other bands used for this construction (*Swift* b , CSP $BVri$ and LCOGT z) have adequate late-time coverage. The projected values are all consistent with the measured upper limits from non-detection in those bands, and the overall contribution of these bands to the bolometric luminosity is small ($< 5\%$) at late times.

At each epoch, we construct a broad-band SED of LSQ12gdj in the observer frame using the natural-system transmission curves, and then de-redshift it to the rest frame, rather than computing full $K + S$ -corrections for all of our broadband photometry. Since we have no detailed UV or NIR time-varying spectroscopic templates for LSQ12gdj, full $K + S$ -corrections are not feasible for all of the *Swift* bands; since we need only the overall bolometric flux over a wide wavelength range instead of rest-frame photometry of individual bands, they are not strictly necessary. We have no NIR photometry of LSQ12gdj either, so we use the NIR template described in Scalzo et al. (2014) to predict the expected rest-frame magnitudes in $YJHK$ band for a SN Ia with $x_1 = 1$. The size of the correction ranges from a minimum of 7% near maximum light to 27% around 35 days after maximum light, comparable to the observed NIR fractions for SN 2007if (Scalzo et al. 2010) and SN 2009dc (Taubenberger et al. 2013).

To determine a piecewise linear observer-frame broadband SED at each epoch, $F(\lambda_j)$, evaluated at the central wavelength λ_j of each band j , we solve the linear system

$$\frac{\int F_n(\lambda) T_j(\lambda) d\lambda}{\int T_j(\lambda) d\lambda} = 10^{-0.4(m_j)}, \quad (2)$$

where m_j is the observed magnitude, and $T_j(\lambda)$ the filter transmission, in band j . The system is represented as a matrix equation $\mathbf{Ax} = \mathbf{b}$, where \mathbf{x} and \mathbf{b} give the flux densities and observations, and \mathbf{A} is the matrix of a linear operator corresponding to

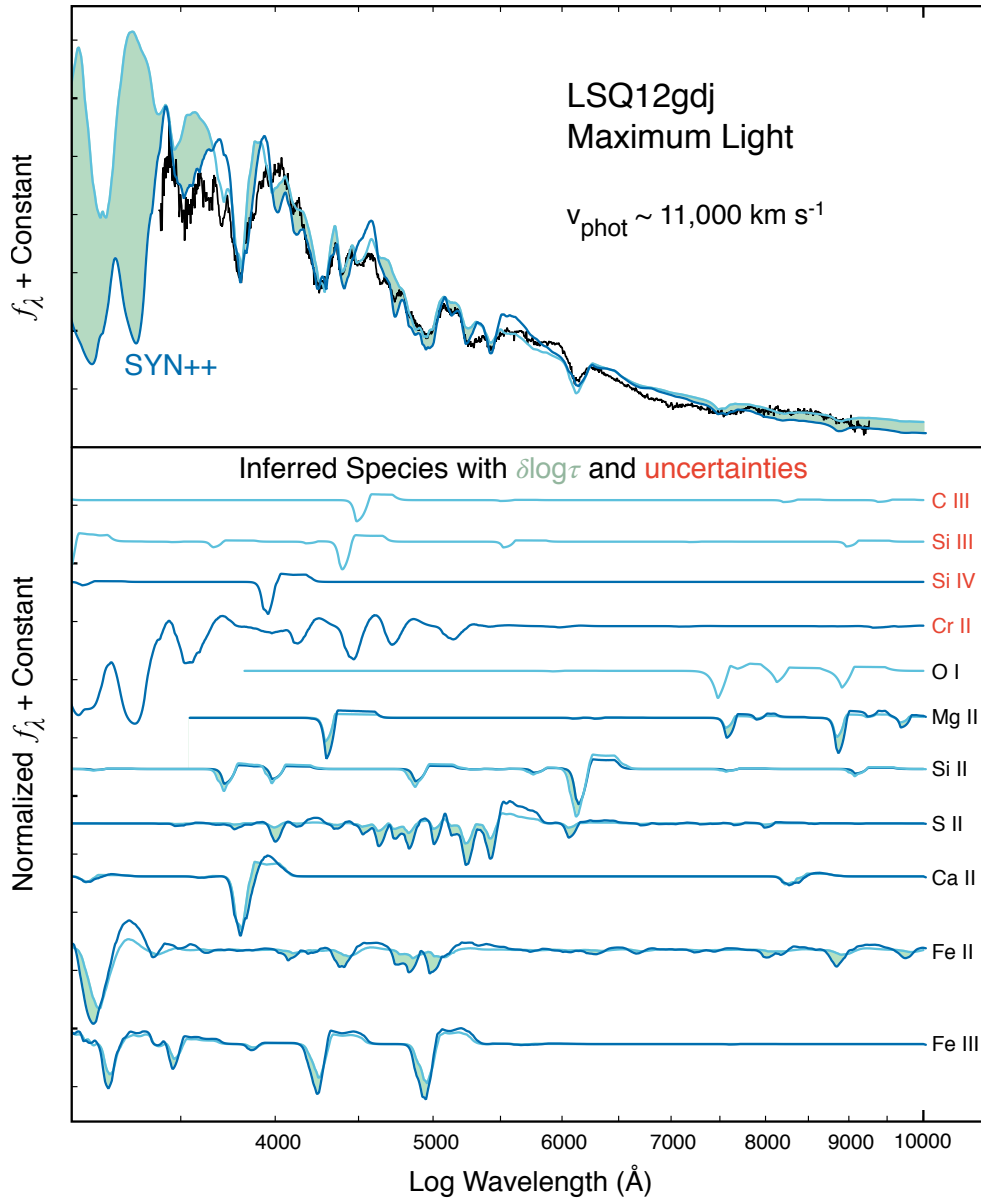


Figure 4. Maximum light SYN++ fit comparisons between two best fits, with and without the inclusion of Cr II. Species listed in red denote degenerate solutions for some observed absorption features, while subsequent uncertainties associated with respective line strengths ($\log \tau$) between our two best fits are represented as a band of aquamarine.

the process of synthesizing photometry. We discretize the integrals via linear interpolation (i.e., the trapezoid rule) between the wavelengths at which the filter transmission curves are measured. We solve the system using nonlinear least squares to ensure positive fluxes everywhere. The Swift *uvw1* and *uvw2* bands have substantial red leaks (Breeveld et al. 2011), but the red-leak flux is strongly constrained by the optical observations, and we find our method can reproduce the original *Swift* magnitudes to within the errors. We exclude Swift *B* and *V* when higher-precision CSP *B* and *V* measurements are available, covering similar wavelength regions. To convert this observer-frame SED to the rest frame, we follow Nugent et al. (2002):

$$f_{\lambda}^z(\lambda) d\lambda = \frac{d\lambda}{1+z} f_{\lambda} \left(\frac{\lambda}{1+z} \right). \quad (3)$$

We integrate the final SED in the window 1550–23000 Å to obtain the bolometric flux. Simulating this procedure end-to-end using *UBVRI* synthetic photometry on SN Ia spectra from the BSNIP sample (Silverman et al. 2012) with phases between -9 and $+460$ days, we find that (for zero reddening) we can reproduce the 3250–8000 Å quasi-bolometric flux to within 1% (RMS). We add this error floor as a systematic error in quadrature to each of our bolometric flux points.

To account for Milky Way and host galaxy extinction, we make bolometric light curves for a grid of possible $E(B - V)$ and R_V values, fixing $R_V = 3.1$ for the Milky Way contribution. We sample $E(B - V)_{\text{host}}$ in 0.01 mag steps from 0.00–0.20 mag, and we sample $R_{V,\text{host}}$ in 0.2 mag/mag steps from 0.0–10.0. We interpolate the light curves linearly on this grid as part of the Monte Carlo sampling described in §4.1, applying our prior

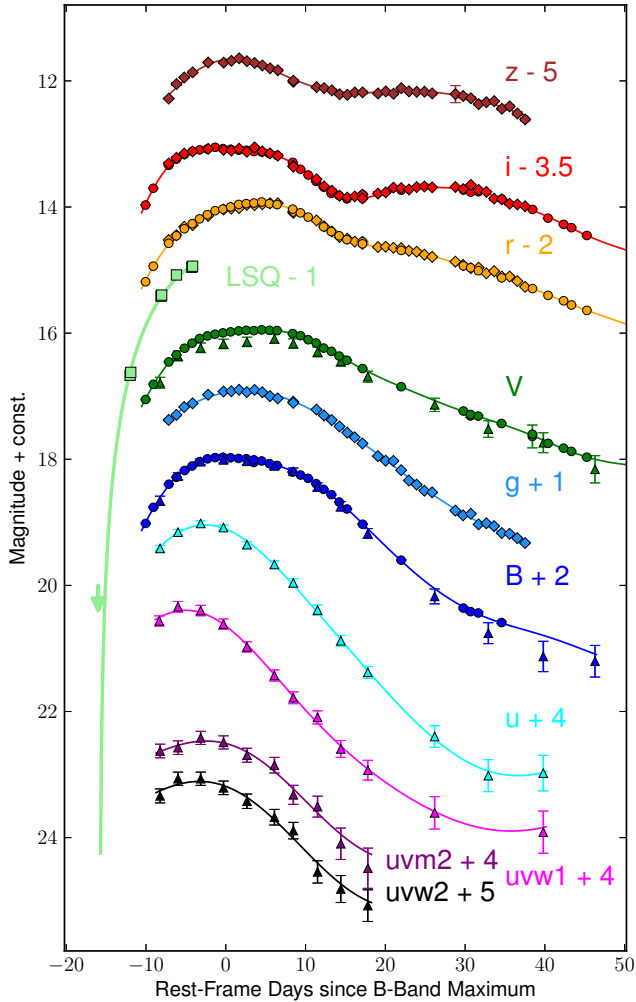


Figure 6. Multi-band light curves of LSQ12gdj. CSP and LCOGT points are shown as circles, *Swift* points are upward-facing triangles, and LSQ points are squares. Solid curves: Gaussian process regression fit to the data (see Rasmussen & Williams 2006; Scalzo et al. 2014), except LSQ, for which the Arnett (1982) functional form is used (well-approximated by a t^2 rise at early times). Light curve phase is with respect to B -band maximum at MJD 56252.5 (2012 Nov 21.5).

on $E(B - V)_{\text{host}}$ and $R_{V,\text{host}}$ given in 3.2 and constraining their values to remain within the grid during the sampling.

Figure 7 shows the resulting time-dependent SED of LSQ12gdj for zero host galaxy reddening. The peak wavelength changes steadily as the ejecta expand and cool, making *Swift* u the most luminous band at early phases. Although a significant fraction of the flux is emitted bluewards of 3300 Å, the flux density cuts off sharply bluewards of *Swift* $uvm2$. Less than 1% of the flux is emitted bluewards of 2300 Å at all epochs, and our SED in these regions is consistent with statistical noise. This behavior is inconsistent with simply being the Rayleigh-Jeans tail of a hot blackbody. Although we have no UV spectroscopy of LSQ12gdj, we expect the sharp cutoff blueward of 3000 Å for the entire rise of the SN to be formed by line blanketing from iron-peak elements (e.g. Cr II, as in Figure 4), as is common in SNe Ia.

Figure 8 shows the bolometric light curve, together with Gaussian process regression fits. Like other candidate super-Chandrasekhar-mass SNe Ia observed with *Swift* (Brown et al.

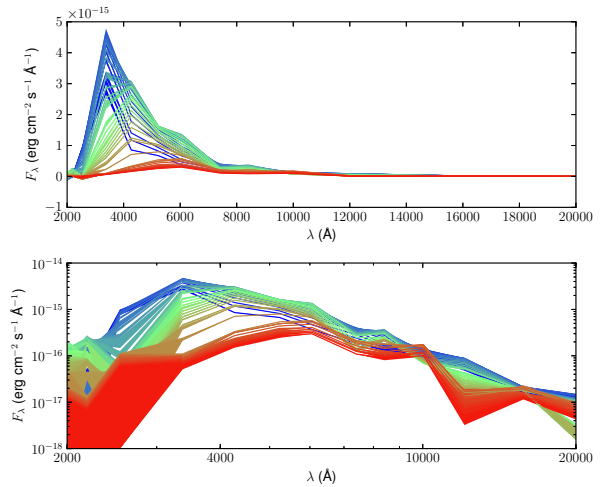


Figure 7. Rest-frame low-resolution SED time series of LSQ12gdj, 1550–23100 Å, constructed from *Swift* UV + CSP $BVR'i'$ photometry. SED colours show the phase, ranging from blue (–10 days) to red (+45 days). Top: linear scale; bottom: log scale. Colored bands represent the 1σ confidence region around the mean.

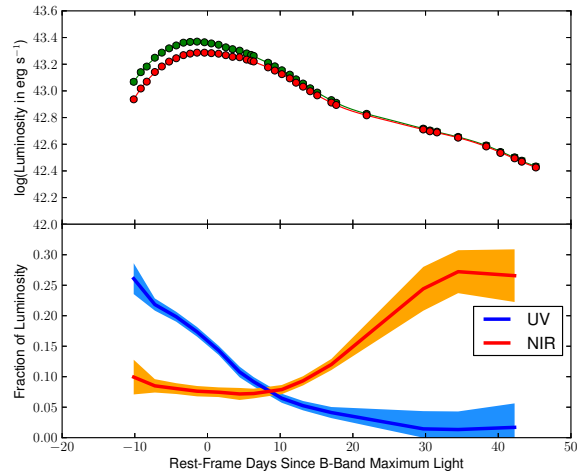


Figure 8. Rest-frame bolometric light curve of LSQ12gdj obtained by integrating the SED of Figure 7. Top: Bolometric light curve 3300–23100 Å (red) and 1550–23100 Å (green) representing the results with and without *Swift* UV, including Gaussian process regression fit (connecting curves). Bottom: Fraction of bolometric flux bluewards of 3300 Å (“UV”) and redwards of 8800 Å (“NIR”, estimated from a template); the solid curves show the mean behavior, and the lighter bands show the 1σ confidence region around the mean.

2014), LSQ12gdj is bright at UV wavelengths from the earliest phases. Up to 27% of the bolometric flux is emitted blueward of 3300 Å at day –10, decreasing to 17% at B -band maximum light and to < 5% by day +20. After day +20, the SN is no longer detected in the *Swift* bands, so the small constant fraction reflects our method of accounting for missing data (with large error bars). For comparison, in the well-observed normal SN Ia 2011fe (Pereira et al. 2013), at most 13% of the luminosity is emitted blueward of 3400 Å, reaching this point 5 days before B -band maximum light; the UV fraction is 9% at day –10, and only 3% at day –15. UV flux contributes only 2% of SN 2011fe’s total luminosity by day +20, and continues to decline thereafter.

4 DISCUSSION

In this section we perform some additional modelling and comparison to interpret our observations of LSQ12gdj. We fit the bolometric light curve in §4.1 to infer the ejected mass and place rough constraints on trapped radiation from interaction with a compact envelope. In §4.2 we attempt to constrain the impact of interaction with an extended CSM wind, including constraints on CSM mass based on blueshifted Na I D absorption (Maguire et al. 2013) and a light curve comparison to known CSM-interacting SNe Ia. Finally, in §4.3 we consider the implications of our findings for the more established super-Chandrasekhar-mass SNe Ia, including SN 2007if and SN 2009dc.

4.1 Modeling of the ^{56}Ni Mass and Ejected Mass

LSQ12gdj has excellent UV/optical coverage from well before maximum to over 40 days after maximum, allowing us to model it in more detail than possible for many other SNe Ia. We use the BOLOMASS code (Scalzo et al., in prep), based on a method applied to other candidate super-Chandrasekhar-mass SNe Ia (Scalzo et al. 2010, 2012), as well as normal SNe Ia (Scalzo et al. 2014). The method constrains the ^{56}Ni mass, M_{Ni} , and the ejected mass, M_{ej} , using data both near maximum and at late times, when the SN is entering the early nebular phase.

BOLOMASS uses the Arnett (1982) light curve model, including as parameters the expected time t_0 at which the ejecta become optically thin to ^{56}Co gamma rays. However, BOLOMASS also calculates the expected transparency of the ejecta to gamma rays from ^{56}Co decay at late times, using the formalism of Jeffery (1999) together with a 1-D parametrized model $\{\rho(v), \mathbf{X}(v)\}$ of the density and composition structure as a function of the ejecta velocity v . The effective opacity for Compton scattering (and subsequent down-conversion) of ^{56}Co -decay gamma rays in the optically thin limit (Swartz et al. 1995) is much more precisely known than optical-wavelength line opacities near maximum light (Khokhlov et al. 1993); this allows BOLOMASS to deliver more robust, quantitative predictions than applications of the Arnett (1982) formalism which ignore Compton scattering and rely on assumed fixed values for the optical-wavelength opacity. BOLOMASS is a Bayesian code, using the affine-invariant Monte Carlo Markov Chain sampler EMCEE (Foreman-Mackey et al. 2013) to sample the model parameters and marginalize over nuisance parameters associated with systematic errors, subject to a suite of priors which encode explosion physics from contemporary explosion models.

The Arnett (1982) light curve model includes as parameters not only M_{Ni} , the light curve shape, and the gamma-ray transparency time t_0 , but estimates of the initial thermal energy E_{th} of the ejecta and the finite size R_0 of the exploding progenitor. They enter through the dimensionless combinations

$$y = \frac{t_{\text{rise}}}{2\tau_{\text{Ni}}} = \frac{t_{\text{rise}}}{17.6 \text{ days}}, \quad (4)$$

$$w = \frac{2R_0}{t_{\text{rise}}v_{\text{KE}}} \sim \frac{R_0}{10^{15} \text{ cm}}. \quad (5)$$

While the typical use of this model for white dwarfs sets $w = 0$, allowing the finite size to float in this case may help us assess the potential contribution of trapped radiation from interaction with a compact, hydrogen-free CSM envelope which might otherwise be invisible (it is not appropriate for an ongoing shock interaction).

Figure 9 shows two possible fits of the Arnett (1982) light curve model to the bolometric light curve of LSQ12gdj. Arnett (1982) points out that the approximations used break down between maximum light and late phases, when the SN is in transition from

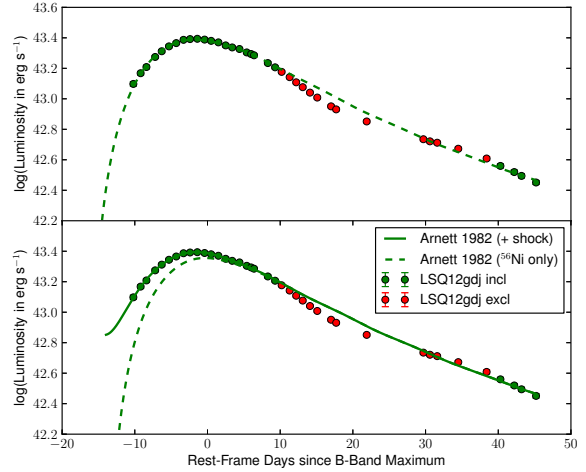


Figure 9. Fits of the Arnett (1982) light curve model to the bolometric light curve of LSQ12gdj, including the trapping of thermalized kinetic energy from an interaction with a compact carbon-oxygen envelope, in the context of the tamped detonation scenario. Top: Zero initial radius. Bottom: Initial radius and thermal energy determined by the fit, showing the full fit (solid curve) and the contribution due only to radioactive decay (dashed curve). Red symbols mark points in the transition regime from photospheric to early nebular phase, which have been excluded from the fit.

full deposition of radioactive decay energy to the optically thin regime. We therefore exclude light curve points between 10 days and 40 days after B -band maximum light, and find that the Arnett (1982) light curve model provides an excellent fit to the remaining points.

When we fix $w = 0$ and consider only the radioactive contribution, we recover $t_{\text{rise}} = 16.4$ days, in agreement with the t^2 fit to the early-phase LSQ data, and $M_{\text{Ni}} = 1.00 M_{\odot}$. Allowing w to float reveals a second possible solution in which trapped thermal energy contributes around 10% of the luminosity at maximum light. The fit has $w = 0.013$ and $E_{\text{th}} = 6 \times 10^{50}$ erg, and has a significantly shorter rise time $t_{\text{rise}} = 14.1$ days, exploding just before the initial detection by LSQ. This value of w corresponds to an effective radius of roughly 10^{13} cm, more extended than the envelopes in the DET2ENVN series (Khokhlov et al. 1993) but not implausibly so for a non-violent merger. The amount of thermalized kinetic energy is compatible with the formation of a reverse-shock shell near 10000 km s^{-1} in a tamped detonation. Importantly, the trapped radiation contributes most at early times and around maximum light, but disappears on a light curve width timescale, just as suggested by Hachinger et al. (2012) and Taubenberger et al. (2013) in the case of SN 2009dc. The late-time behavior is the same as for the radioactive-only case, and the best-fit ^{56}Ni mass is $0.88 M_{\odot}$. The reduced chi-square for both fits are very low (0.47 for $w = 0$ versus 0.15 for $w > 0$), so that while the $w > 0$ fit is favored slightly, both are consistent with our observations.

The ejected mass estimate depends on the actual density structure and ^{56}Ni distribution in the ejecta. We consider two possible functional forms for the density structure, one which depends exponentially on velocity and one with a power-law dependence, as in Scalzo et al. (2014). We parametrize the stratification of the ejecta by a mixing scale a_{Ni} (Kasen 2006), and consider stratified cases with $a_{\text{Ni}} = 0.1$ and well-mixed cases with $a_{\text{Ni}} = 0.5$. The detailed model-dependence of the trapping of radiation near maximum light is often factored out into a dimensionless ratio α (Nugent et al. 1995; Howell et al. 2006, 2009) of order unity, by which the rough

Table 4. Ejected mass and ^{56}Ni mass of LSQ12gdj under various priors

Run	$\rho(v)^a$	a_{Ni}^b	v_{KE}^c (km s $^{-1}$)	$M_{\text{ej}}/M_{\odot}^d$	P_{Sch}^e
A	pow3x3	0.5	10390 $^{+634}_{-284}$	1.56 $^{+0.13}_{-0.08}$	0.992
B	pow3x3	0.1	10484 $^{+613}_{-295}$	1.51 $^{+0.10}_{-0.07}$	0.953
C	exp	0.5	10713 $^{+503}_{-250}$	1.43 $^{+0.08}_{-0.05}$	0.691
D	exp	0.1	10939 $^{+485}_{-292}$	1.38 $^{+0.06}_{-0.07}$	0.354

^a Assumed density profile as a function of ejecta velocity: “exp” $\propto \exp(-\sqrt{12}v/v_{\text{KE}})$, as in 1-D explosion models. “pow3x3” $\propto [1 + (v/v_{\text{KE}})^3]^{-3}$, similar to 3-D models cited in Scalzo et al. (2014).

^b Assumed width of the mixing layer near the iron-peak core boundary, in mass fraction; 0.1 is highly stratified while 0.5 is well-mixed (Kasen 2006).

^c Kinetic energy scaling velocity. ^d Total ejected mass.

^e Fraction of the integrated probability density lying above

$M_{\text{ej}} = 1.4 M_{\odot}$.

“Arnett’s rule” estimate of M_{Ni} from the maximum-light luminosity is divided. Here we use the Arnett light curve fit directly to estimate the ^{56}Ni mass and the amount of thermalized kinetic energy trapped and released, resulting in an effective α between 1.0 and 1.1 for LSQ12gdj. For the $w = 0$ Arnett formalism, $\alpha = 1$ by construction, ignoring both opacity variation in the ejecta and/or less than complete gamma-ray deposition near maximum light (Blondin et al. 2013). In all reconstructions, we allow the unburned carbon/oxygen fraction, the envelope size, and the thermalized kinetic energy to float freely, and we assume that neutronized material does not form a ^{56}Ni -free “hole” in the center of the ejecta, as is found in multi-dimensional explosion models (Krueger et al. 2012; Seitenzahl et al. 2013).

Table 4 shows the inferred M_{ej} and probability of exceeding the Chandrasekhar limit for four different combinations of priors, marginalizing over the full allowed range of w and E_{th} . The full Monte Carlo analysis robustly predicts $t_{\text{rise}} = 16 \pm 1$ days and $M_{\text{Ni}} = 0.96 \pm 0.07 M_{\odot}$. The thermalized kinetic energy is constrained to be less than about 10^{51} erg; this maximum value results in ejecta with a *maximum* velocity around 10000 km s $^{-1}$, roughly consistent with our observations. The well-mixed models have M_{ej} larger by about $0.07 M_{\odot}$ than the stratified models, and slightly larger uncertainties. Models with power-law density profiles have M_{ej} larger by about $0.14 M_{\odot}$ than models with exponential density profiles. The exponential density profile, typical of one-dimensional models such as W7 (Nomoto et al. 1984), consistently underestimates the ejected mass when applied to three-dimensional explosion models of SNe Ia with a variety of ejected masses Scalzo et al. (2014); this lends circumstantial, but not conclusive, weight to the power-law profile estimates, which tell us that LSQ12gdj is super-Chandrasekhar-mass. Although BOLO-MASS can model any user-defined spherically symmetric density structure, the light curve is sensitive primarily to the total Compton scattering optical depth, and not directly to the actual ejecta density profile, for all but the most highly disturbed density structures.

Our judgment as to whether LSQ12gdj is actually super-Chandrasekhar-mass hinges on our interpretation of its origin. If LSQ12gdj is indeed a tamped detonation, it is probably (slightly) super-Chandrasekhar-mass, and could be explained by a Chandrasekhar-mass detonation inside a compact envelope of mass around $0.1 M_{\odot}$. If all of LSQ12gdj’s luminosity is due to radioactive energy release, it could be (slightly) sub-Chandrasekhar-mass, a good candidate for a double det-

onation (Woosley & Weaver 1994; Fink et al. 2010) of about $1.3 M_{\odot}$, or a conventional Chandrasekhar-mass near-pure detonation (Blondin et al. 2013; Seitenzahl et al. 2013). Interestingly, the DDC0 model of Blondin et al. (2013) has a rise time of 15.7 days, very close to the value we observe. The tamped detonation interpretation has the advantage of explaining why LSQ12gdj is UV-bright and spectroscopically peculiar before maximum light, while other SNe Ia which appear to have comparable M_{Ni} may appear spectroscopically normal (Scalzo et al. 2014). One should keep in mind that the Arnett (1982) formalism is an approximate treatment and neglects many details of radiation trapping, including the potential for a “dark phase” (Piro & Nakar 2013), as mentioned in §3.2.

4.2 Constraints on Ongoing Shock Interaction

We also address the question of whether LSQ12gdj might be undergoing shock interaction with a hydrogen-poor extended wind, adding luminosity to its late-time light curve. The “Ia-CSM” events, such as SN 2002ic (Hamuy et al. 2003), SN 2005gj (Aldering et al. 2006; Prieto et al. 2007), SN 2008J (Taddia et al. 2012), and PTF11kx (Dilday et al. 2012), have spectra which seem to be well-fit by a combination of a 1991T-like SN Ia spectrum, a broad continuum formed at the shock front, and narrow H α lines formed in photoionized CSM (Silverman et al. 2013a,b; Leloudas et al. 2013). A hydrogen-poor extended CSM could produce pseudocontinuum luminosity and weaken absorption lines via toplighting (Branch et al. 2000), while not producing any distinctive line features itself, although a very massive envelope could in principle produce carbon or oxygen lines (Ben-Ami et al. 2014).

Figure 10 shows the g -band light curve of LSQ12gdj alongside those of the Ia-CSM SN 2005gj and PTF11kx, the super-Chandrasekhar-mass SN 2007if, the 1991T-like SN 2005M, and the fast-declining, spectroscopically normal SN 2004eo. We choose g for the comparison because it is the bluest band observed (or synthesizable) in common for all of the SNe. SN 2005gj, the clearest example of ongoing shock interaction, declines extremely slowly, with far more luminosity at day +40 and later than any of the other SNe. PTF11kx, a case of an intermediate-strength shock interaction, has peak brightness comparable to the 1991T-like SN 2005M, but shows a long tail of shock interaction luminosity and is up to 0.5 mag more luminous than SN 2005M at day +60. By a year after explosion, the spectrum of PTF11kx, like that of SN 2005gj, is dominated by shock interaction signatures such as H α (Silverman et al. 2013a), rather than by Fe II as for SN 2007if (Taubenberger et al. 2013).

Despite having peak magnitudes that differ over a range of 1 mag, SN 2005M, SN 2007if, and LSQ12gdj all have very similar post-maximum light curve shapes, more consistent with each other than with the Ia-CSM. This puts strong constraints on the density and geometry of any CSM present; existing examples of Ia-CSM show that the light curve shapes can vary dramatically according to the density and geometry of the surrounding medium. In particular, none of the SNe Ia-91T show an extended power-law tail to the light curve, nor do they match expectations from radiation hydrodynamics simulations of heavily enshrouded SNe Ia in hydrogen-poor envelopes (Fryer et al. 2010; Blinnikov & Sorokina 2010).

We can derive a more quantitative upper limit on the presence of extended CSM by searching for circumstellar Na I D absorption. Maguire et al. (2013) observed LSQ12gdj with the XSHOOTER spectrograph on the ESO Very Large Telescope at Paranal, finding narrow Na I D and Ca II H+K absorption blueshifted at -220 km s $^{-1}$ relative to the recessional velocity of the LSQ12gdj host. LSQ12gdj is one of a larger sam-

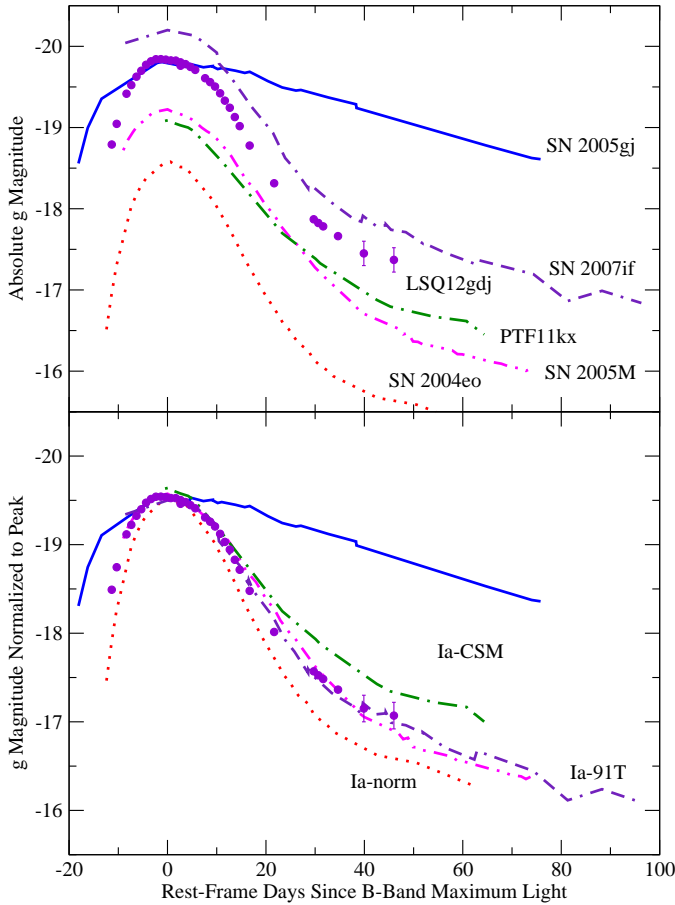


Figure 10. Comparison of g -band light curves of peculiar SNe Ia. The CSP and *Swift* B -band light curves of LSQ12gdj (filled circles) have been S -corrected to g band using the spectra in this paper. References for the other light curves include: SN 2005gj, from Prieto et al. (2007) (solid curve); PTF11kx, from Dilday et al. (2012) (dash-dot curve); SN 2004eo and SN 2005M, from Contreras et al. (2010) (dotted and dash-dot-dot curves); and SN 2007if, from Stritzinger et al. (2012) and Scalzo et al. (2010) (dash-dot curve).

ple of SNe Ia with blueshifted absorption features studied in Maguire et al. (2013). While blueshifted Na I D absorption would be expected statistically for a population of progenitors surrounded by a CSM wind, of either single-degenerate (Sternberg et al. 2011) or double-degenerate (Shen et al. 2012; Raskin & Kasen 2013) origin, we have no way of knowing whether such absorption is circumstellar for any individual SN Ia, or whether it arises from interstellar material in the host galaxy.

We can nevertheless derive a conservative upper limit assuming all of the absorption arises from hydrogen-rich CSM. Since $EW(\text{Na I D})$ near the host galaxy redshift is small, there should be little CSM present around LSQ12gdj. We use the VPFIT^4 code to place an upper limit on the column density of Na I using the XSHOOTER spectrum from Maguire et al. (2013), in the case in which all Na I D absorption is circumstellar; we obtain $N(\text{Na I}) < 4 \times 10^{11} \text{ cm}^{-2}$. For a thin spherical shell of radius 10^{16} cm , thickness 10^{14} cm , and H -rich composition of solar metallicity ($\log(\text{Na}/\text{H}) + 12 = 6.17$; Asplund et al. 2005) undergoing complete recombination of Na I, similar to the treatment

⁴ VPFIT was developed by R. F. Carswell and can be downloaded for free at <http://www.ast.cam.ac.uk/~rfc/vpfit.html>.

of SN 2006X in Patat et al. (2007), we obtain a CSM shell mass $M_{\text{env}} < 3 \times 10^{-7} M_{\odot}$. Similar limits can be obtained by multiplying the upper limit on the hydrogen column density by the surface area of a sphere of radius 10^{16} cm ($6 \times 10^{-7} M_{\odot}$), or by using the estimated fluence of ionizing photons from Patat et al. (2007) ($6 \times 10^{-7} M_{\odot}$). The known H -rich SNe Ia-CSM, such as SN 2005gj, have estimated electron densities and CSM masses several orders of magnitude higher (Aldering et al. 2006), as do the total CSM masses ejected in the tidal tails of the mergers simulated by Raskin & Kasen (2013).

These estimates, of course, assume hydrogen-rich CSM, whereas shock-powered models for super-Chandrasekhar-mass SNe Ia posit CSM rich in helium or even carbon (Hachinger et al. 2012; Taubenberger et al. 2013). The first ionization potentials for carbon (11.3 eV) and oxygen (13.6 eV) are comparable to that of hydrogen, so one might expect similar electron densities from photoionization in those cases; however, the expected relative abundance of sodium in such material is highly uncertain, making it difficult to set definite limits. For helium the ionization potential is much higher (24.6 eV), requiring hard UV flux blueward of 500 \AA ; this entirely precludes useful limits from Na I D absorption for CSM composed predominantly of helium.

To summarize, we have compiled the following lines of evidence regarding CSM interaction in LSQ12gdj:

- (i) Since LSQ12gdj is clearly typed as a SN Ia near maximum light, any CSM by this time either must be optically thin or must not cover the entire photosphere. The fraction of luminosity which can be produced by shock heating or other non-radioactive sources is limited to about 75% of the total (Leloudas et al. 2013).
- (ii) The weak Na I D absorption limits the mass of extended hydrogen-rich CSM around LSQ12gdj to be less than $\sim 10^{-6} M_{\odot}$.
- (iii) An extended all-helium or carbon-oxygen CSM could in theory evade the Na I D constraints, but would probably produce a lingering power-law tail to the light curve, as in SN 2005gj or PTF11kx, which we do not see in LSQ12gdj.
- (iv) Fits to the bolometric light curve of LSQ12gdj limit the size of any compact envelope to be $< 10^{13} \text{ cm}$. In this case the interaction would be frozen out before the first detection, resulting in all intermediate-mass elements being swept up into a reverse-shock shell and producing the very low velocity gradient observed.
- (v) If LSQ12gdj has a compact envelope, its relatively high Si II velocity implies a light envelope of mass $\sim 0.1 M_{\odot}$; this traps some radiation, but not as much as might be trapped in a heavily enshrouded explosion.

It seems therefore that while some CSM may be present around LSQ12gdj, luminosity from ongoing shock interaction is negligible. Without tell-tale emission lines, however, the composition of the CSM and the evidence for a single-degenerate origin for LSQ12gdj remain ambiguous.

4.3 Implications for SN 2007if and SN 2009dc

LSQ12gdj was flagged early in its evolution as a bright, peculiar SN Ia. By considering the UV contribution to LSQ12gdj's luminosity, we have shown that up to 10% of LSQ12gdj's maximum-light luminosity may be trapped thermal energy from an interaction with a compact envelope. It is likely that such a model, with small variations in the relative contributions of ^{56}Ni mass and radioactivity to the maximum-light luminosity, can explain the observational appearance of all 1991T-like SNe Ia of comparable luminosity, including SN 1991T itself and the SNe Ia analyzed in Scalzo et al.

(2012). We now consider what lessons may extend to the much brighter SNe Ia, SN 2007if and SN 2009dc, if any.

SN 2007if was notable not only for its extreme luminosity, but for its low photospheric velocity (9000 km s^{-1}) near maximum light. Scalzo et al. (2010) found that these properties were incompatible with a normal density structure, and proposed that SN 2007if must have been a tamped detonation with a relatively high-mass ($0.4 M_{\odot}$) envelope. The analysis used $\alpha = 1.3 \pm 0.1$, i.e., it assumed that around 30% of SN 2007if’s maximum-light luminosity was trapped radiation, and a long rise time of 23 days. While the rising part of the light curve was well-sampled by ROTSE-III (Yuan et al. 2010), with the first detection at 20 days before *B*-band maximum light, SN 2007if has only one pre-maximum bolometric light curve point, making its maximum-light colour uncertain (Scalzo et al. 2012) and precluding a more detailed analysis of the pre-maximum light curve.

Crucially, SN 2007if also has no UV data. If the UV component of SN 2007if’s bolometric luminosity evolved in a similar way to LSQ12gdj’s, this would have made SN 2007if 17% more luminous at peak ($3.7 \times 10^{43} \text{ erg s}^{-1}$), requiring a ^{56}Ni mass of around $(2.0/\alpha) M_{\odot}$. Such extreme explosions are still achievable under some models for super-Chandrasekhar-mass SNe Ia, such as collisions of carbon-oxygen white dwarfs (Raskin et al. 2010) or pure detonations of differentially rotating white dwarfs (Pfannes et al. 2010b), but are at the outer limit of what can be achieved with state-of-the-art numerical models of exploding white dwarfs. We already have good evidence that SN 2007if has a disturbed density structure and that at least some of its maximum-light radiation must be trapped, thermalized kinetic energy, but it is not difficult to imagine that the precise fraction could be larger than 30%. Regardless, most of that radiation should be gone by around 60 days after explosion, so the late-time light curve measurements correctly reflect that the ejecta must have been extremely massive. If we assume $\alpha = 2.0$, bringing M_{Ni} down to $1.0 M_{\odot}$, the limit of what can be achieved in a Chandrasekhar-mass explosion (Khokhlov et al. 1993), we must still have $M_{\text{ej}} > 2.26 M_{\odot}$ at 99% confidence.

Similar considerations apply to SN 2009dc, which has an almost identical light curve to SN 2007if out to 100 days past maximum light. SN 2009dc also has *Swift* data (Silverman et al. 2011), though none before maximum light, so the precise shape of its pre-maximum bolometric light curve is still subject to large uncertainties. At maximum light, Silverman et al. (2011) estimate that about 20% of SN 2009dc’s bolometric flux is emitted in the UV. The low IME absorption-line velocities make it impossible for SN 2009dc to have a “normal” density structure, or even much burned material beyond about 9000 km s^{-1} . For SN 2009dc to have been a tamped detonation, the carbon-oxygen envelope must have represented a much larger fraction of the total ejecta mass — possibly as high as 30% of the total — in order to reproduce its even lower ejecta velocities. Under these conditions, the reverse shock should penetrate far into the inner layers of ejecta before stalling, and the distribution of material in the reverse-shock shell becomes important to gamma-ray transport at late times. Thus the approximation previously used by Scalzo et al. (2012) for SN 2007if and other super-Chandrasekhar-mass candidates, in which the shock redistributes kinetic energy and traps thermal energy but has little effect on the late-time light curve, probably breaks down for SN 2009dc.

SN 2009dc’s relatively large ($\sim 75 \text{ km s}^{-1} \text{ day}^{-1}$) Si II velocity gradient presents a problem for the tamped detonation scenario, because no plateau is evident and it is clear that intermediate-mass elements cannot all be trapped in a thin layer. However, given the strength of the shock necessary, the approximation of the reverse-shock shell as a thin layer could also break down here.

Other explosion models, such as pulsating delayed detonations (Khokhlov et al. 1993), could also have given SN 2009dc a highly disturbed density structure without the need for an envelope or for a very narrow layer of intermediate-mass elements in velocity space. Baron et al. (2012) invoked such a model for the slow-declining SN 2001ay (Krisciunas et al. 2011). One difficulty with pulsating models for SN 2009dc is that the shock would freeze out much sooner after explosion than in the case of a tamped detonation, forcing $w = 0$ and preventing a significant contribution to the maximum-light luminosity (but potentially further enhancing trapping of radioactive energy near maximum light).

We should note that while our technique assumes spherically symmetric ejecta, many numerical explosion models of super-Chandrasekhar-mass SNe Ia are highly asymmetric, with preferred rotation, collision, or ignition axes. Asymmetries in the distribution of ^{56}Ni can produce variations in temperature, ionization, and overall luminosity among different lines of sight; for example, the brightest view of the highly asymmetric, $2-M_{\odot}$ violent merger 11+09 (?) was 0.6 mag (bolometric) brighter at peak, and had a rise time 4 days longer, than the faintest view. The effective value of α for the brightest view of 11+09 is 1.8, while that for the faintest view is 0.6. While it is hard to say how significant these effects are for SN 2007if and SN 2009dc without reference to a particular numerical explosion model, the null polarization results for SN 2009dc (Tanaka et al. 2010) imply that SN 2009dc must at least be viewed along a symmetry axis. In a scenario in which variation with viewing angle is used to account for a large fraction of the near-maximum luminosity, bright SNe Ia such as SN 2007if and SN 2009dc should be balanced by fainter super-Chandrasekhar-mass SNe Ia viewed along other angles, which are not detected (Scalzo et al. 2014). Furthermore, the influence of asymmetries on peak brightness should decrease with increasing ^{56}Ni mass fraction (e.g., Maeda et al. 2011), and should lessen gradually as the SN enters the nebular phase and the ejecta become fully transparent.

Finally, Leloudas et al. (2013) show a strong association between 1991T-like SNe Ia and the growing Ia-CSM subclass which show narrow $\text{H}\alpha$ lines in their spectra (Silverman et al. 2013b); they imply that 1991T-like SNe Ia must in general be single-degenerate explosions, although not all of them are required to display strong CSM interaction. Single-degenerate channels for producing super-Chandrasekhar-mass SN Ia progenitors have been proposed (Justham 2011; Hachisu et al. 2011), and SN 2007if and SN 2009dc could in principle be among them. Since the ongoing shock interaction prevents use of the bolometric light curve to measure radioactive decay in Ia-CSM, constraints on their ejected masses must await more detailed modelling, or must be inferred indirectly from those events which show little CSM interaction.

5 CONCLUSIONS

LSQ12gdj is a well-observed, overluminous SN Ia in a nearby galaxy with little to no dust extinction. The extensive spectroscopic time series show that LSQ12gdj is spectroscopically 1991T-like, with intermediate-mass element absorption signatures only in a narrow range of velocities, much like SN 2007if and other 1991T-like SNe Ia Scalzo et al. (2010, 2012). From the bolometric light curve of LSQ12gdj we infer a ^{56}Ni mass of about $0.9 M_{\odot}$ and an ejected mass near the Chandrasekhar mass. LSQ12gdj is likely either a nearly pure Chandrasekhar-mass detonation or a slightly super-Chandrasekhar-mass tamped detonation.

Observations at UV wavelengths well before maximum light provide additional useful constraints on the properties of LSQ12gdj and other 1991T-like SNe Ia, not considered elsewhere. A large

fraction (17%) of the bolometric luminosity near maximum light, and nearly 30% in the earliest observations, is emitted bluewards of 3300 Å. Accounting for this effect increases the derived ^{56}Ni mass significantly relative to cases in which it is ignored (e.g., Scalzo et al. 2012), assuming that the SN is powered through radioactivity alone. Our excellent time and wavelength coverage also allow us to constrain the tamped detonation scenario in detail, confirming that at most 10% of the luminosity comes from trapped thermal energy near maximum light, and almost none at late times.

Our findings represent what can be done with detailed observations, and to push our understanding of super-Chandrasekhar-mass SNe Ia forward, even more detailed observations will be needed. Early ultraviolet coverage is critical, starting as soon after explosion as possible. Optical and near-infrared observations extending to late times, well past maximum light, are needed to place helpful constraints on the mass. Nebular spectra can elucidate the density structure of the innermost ejecta, with implications for the importance of radiation trapping near maximum light. These observations must go hand in hand with sophisticated, self-consistent modelling which can deal with theoretical uncertainties and with systematic errors in the observations.

Measurement of the properties of a general spectroscopically selected sample of 1991T-like SNe Ia could provide vital clues to the identity of their progenitors and how they relate to other super-Chandrasekhar-mass SNe Ia, such as SN 2006gz and SN 2009dc, and to CSM-interacting SNe Ia, such as SN 2005gj and PTF11kx. Such an investigation will complement a similar analysis of a SN Ia sample from an untargeted search selected only by peak absolute magnitude, to determine the spectroscopic diversity and range of explosion mechanisms which can account for superluminous SNe Ia, and how many superluminous SNe Ia result from the explosions of super-Chandrasekhar-mass white dwarfs.

ACKNOWLEDGMENTS

PyRAF and PyFITS are products of the Space Telescope Science Institute, which is operated by AURA for NASA. This research has made use of the NASA/IPAC Extragalactic Database (NED) which is operated by the Jet Propulsion Laboratory, California Institute of Technology, under contract with the National Aeronautics and Space Administration. This research is based on observations collected at the European Organisation for Astronomical Research in the Southern Hemisphere, Chile as part of PESSTO (the Public ESO Spectroscopic Survey for Transient Objects), ESO program ID 188.D-3003. Research leading to these results has received funding from the European Research Council under the European Union’s Seventh Framework Programme (FP7/2007-2013)/ERC Grant agreement n° [291222] (PI : S. J. Smartt). The National Energy Research Scientific Computing Center, supported by the Office of Science of the U.S. Department of Energy under Contract No. DE-AC02-05CH11231, provided staff, computational resources, and data storage for this project. Parts of this research were conducted by the Australian Research Council Centre of Excellence for All-Sky Astrophysics (CAASTRO), through project number CE110001020. This material is also based upon work supported by NSF under grants AST-0306969, AST-0607438 and AST-1008343. RS acknowledges support from ARC Laureate Grant FL0992131. ST acknowledges support from the Transregional Collaborative Research Center TRR 33 “The Dark Universe” of the Deutsche Forschungsgemeinschaft. KM is supported by a Marie Curie Intra European Fellowship, within the 7th European Community Framework Programme (FP7). MF is supported by the European Union FP7 programme through ERC grant

number 320360. MS and CC gratefully acknowledge generous support provided by the Danish Agency for Science and Technology and Innovation realized through a Sapere Aude Level 2 grant. AG acknowledges support by the EU/FP7 via ERC grant no. 307260, a GIF grant, the Minerva ARCHES award and the Kimmel award.

REFERENCES

- Ade, P. A. R., Aghanim, N., Armitage-Caplan, C., et al. 2013, arXiv:1303.5076
- Aldering, G., Antilogus, P., Bailey, S., et al. 2006, *ApJ*, 650, 510
- Arnett, W. D. 1982, *ApJ*, 253, 785
- Asplund, M., Grevesse, N., & Sauval, A. J. 2005, in *Cosmic Abundances as Records of Stellar Evolution and Nucleosynthesis*, ed. F. N. Bash, & T. G. Barnes, p. 25
- Bailey, S., Aldering, G., Antilogus, P., et al. 2009, *A&A*, 500, L17
- Baltay, C., Rabinowitz, D., Hadjijska, E., et al. 2013, *PASP*, 125, 683
- Baron, E., Höflich, P., Krisciunas, K., et al. 2012, *ApJ*, 753, 105
- 2014, *ApJ*, 785, 37
- Benetti, S., Cappellaro, E., Mazzali, P., et al. 2005, *ApJ*, 623, 1011
- Bertin, E. & Arnouts, S. 1996, *A&AS*, 317, 393
- Bertin, E., Mellier, Y., Radovich, M., et al. 2002, *ASP Conference Series*, Vol. 281, eds. D.A. Bohlender, D. Durand, & T.H. Handley, p. 228.
- Blinnikov, S. I. & Sorokina, E. I. 2010, arXiv:1009.4353
- Blondin, S., & Tonry, J. L. 2007, *ApJ*, 666, 1024
- Blondin, S., Dessart, L., Hillier, D. J., et al. 2013, *MNRAS*, 429, 2127
- Branch, D., Fisher, A., & Nugent, P. 1993, *AJ*, 106, 2383
- Branch, D., Jeffery, D. J., Blaylock, M., et al. 2000, *PASP*, 112, 217
- Branch, D., Dang, L., Hall, N., et al. 2006, *PASP*, 118, 560
- Branch, D., Troxel, M. A., Jeffery, D. J., et al. 2007, *PASP*, 119, 135
- Branch, D., Jeffery, D. J., Parrent, J., et al. 2008, *PASP*, 120, 135
- Breeveld, A. A., Landsman, W., Holland, S. T., et al. 2011, in *AIP Conf. Proc. 1358, Gamma-Ray Bursts 2010*, ed. J. E. McEnery, J. L. Racusin, & N. Gehrels (Melville, NY: AIP), 373; arXiv:1102.4717
- Brown, P., Holland, S., Immler, S., et al. 2009, *AJ*, 137, 4517
- Brown, P., Holland, S., & Milne, P. 2014, *ApJ*, in press (arXiv:1404:0650)
- Cardelli, J. A., Clayton, G. C. & Mathis, J. S. 1988, *ApJ*, 329, L33
- Cellier-Holzem, F., Canto, A., Antilogus, P., et al. 2012, *ATEL #4566*
- Childress, M., Scalzo, R. A., Sim, S. A., et al. 2013, *ApJ*, 770, 29
- Childress, M. 2014, *Ap&SS*, 349, 617
- Conley, A., Sullivan, M., Hsiao, E. Y., et al. 2008, *ApJ*, 681, 482
- Contreras, C., Hamuy, M., Phillips, M. M. 2010, *AJ*, 139, 519
- Das, U. & Mukhopadhyay, B. 2013, *Phys. Rev. Lett.*, 110, 071102
- Das, U. & Mukhopadhyay, B. 2013, *ApJ*, 767, L14
- Dilday, B., Howell, D. A., Cenko, S. B., et al. 2012, *Science*, 337, 942
- Di Nella, H., Couch, W. J., Paturel, G., et al. 1996, *MNRAS*, 283, 367
- Di Stefano, R. & Kilic, M. 2012, *ApJ*, 759, 56
- Fink, M., Röpke, F. K., Hillebrandt, W., et al. 2010, *A&A*, 514, A53
- Filippenko, A. V., Richmond, M. W., Matheson, T., et al. 1992, *ApJ*, 384, L15
- Folatelli, G., Phillips, M. M., Burns, C., R., et al. 2010, *AJ*, 139, 120
- Foley, R. J. & Kasen, D. 2010, *ApJ*, 729, 55
- Foreman-Mackey, D., Hogg, D. W., Lang, D., et al. 2013, *PASP*, 125, 306
- Fryer, C. L., Ruiter, A. J., Belczynski, K., et al. 2010, *ApJ*, 725, 296
- Fukugita, M., Ichikawa, T., Gunn, J. E., et al. 1996, *AJ*, 111, 1748
- Ganeshalingam, M., Li, W., & Filippenko, A. V. 2011, *MNRAS*, 416, 2607
- Goldhaber, G., Groom, D. E., Kim, A. G., et al. 2001, *ApJ*, 558, 359
- Guy, J., Astier, P., Baumont, S., et al. 2007, *A&A*, 466, 11
- Guy, J., Sullivan, M., Conley, A., et al. 2010, *A&A*, 523, 7
- Hachinger, S., Mazzali, P., Taubenberger, S., et al. 2012, *MNRAS*, 427, 2057
- Hachisu, I., Kato, M., Saio, H., et al. 2012, *ApJ*, 744, 69
- Hamuy, M., Phillips, M. M., Suntzeff, N., et al. 2003, *Nature*, 424, 651
- Hamuy, M., Folatelli, G., Morrell, N. I., et al. 2006, *PASP*, 118, 2
- Hicken, M., Garnavich, P. M., Prieto, J. L., et al. 2007, *ApJ*, 669, L17
- Hillebrandt, W., Sim, S. A., & Röpke, F. K. 2007, *A&A*, 465, L17
- Höflich, P. & Khokhlov, A. 1996, *ApJ*, 457, 500
- Howell, D. A., Sullivan, M., Nugent, P. E., et al. 2006, *Nature*, 443, 308

- Howell, D. A. et al. 2009, ApJ, 691, 661
- Iben, I. & Tutukov, A. V. 1984, ApJS, 54, 335
- Jeffery, D. J. 1999, arXiv:astro-ph/9907015
- Justham, S. 2011, ApJ, 730, L34
- Kasen, D. 2006, ApJ, 649, 939
- Khokhlov, A., Müller, E. & Höflich, P. 1993, A&A, 270, 223
- Krisciunas, K., Li, W., Matheson, T., et al. 2011, AJ, 142, 74
- Krueger, B. K. Jackson, A. P., Townsley, D. M., et al. 2012, ApJ, 757, 175
- Landolt, A. U. 1992, AJ, 104, 340
- Lantz, B., Aldering, G., Antilogus, P., et al. 2004, Proc. SPIE, 5249, 146
- Leloudas, G., Hsiao, E. Y., Johansson, J., et al. 2013, A&A, submitted (arXiv:1306.1549)
- Maeda, K., Kawabata, K., Li, W., et al. 2009, ApJ, 690, 1745
- Maeda, K., Leloudas, S., Taubenberger, S., et al. 2011, MNRAS, 413, 3075
- Maguire, K., Sullivan, M., et al. 2013, MNRAS, 436, 222
- Nomoto, K., Thielemann, F.-K., & Yokoi, K. 1984, ApJ, 286, 644
- Nugent, P., Branch, D., Baron, E., et al. 1995, Phys. Rev. Lett., 75, 394
- Nugent, P. E., Kim, A. G., & Perlmutter, S. 2002, PASP, 114, 803
- Patat, F., Chandra, P., Chevalier, R., et al. 2007, Science, 317, 924
- Pedregosa, F., Varoquaux, G., Gramfort, A., et al. 2011, JMLR, 12, 2825
- Pereira, R., Aldering, G., Antilogus, P. 2013, A&A, 554, 27
- Perlmutter, S., Aldering, G., Goldhaber, G., et al. 1999, ApJ, 517, 565
- Pfannes, J. M. M. Niemeyer, J., & Schmidt, W. 2010, A&A, 509, 75
- Phillips, M. M., Wells, L. A., Suntzeff, N. B., et al. 1992, AJ, 103, 1632
- Phillips, M. M., Lira, P., Suntzeff, N. B., et al. 1999, AJ, 118, 1766
- Piro, A. L., & Nakar, E. 2013, ApJ, 769, 67
- Piro, A. L., & Nakar, E. 2014, ApJ, 784, 85
- Prieto, J., Garnavich, P., Phillips, M. M., et al. 2007, arXiv:0706.4088
- Raskin, C., Scannapieco, E., Rockefeller, G., et al. 2010, ApJ, 724, 111
- Raskin, C., & Kasen, D. 2013, ApJ, 772, 1
- Rasmussen, C. E. & Williams, C. K. I., 2006, *Gaussian Processes for Machine Learning*, MIT Press
- Riess, A. G., Press, W. H., & Kirshner, R. P. 1996, ApJ, 473, 88
- Riess, A. G., Filippenko, A. V., Challis, P., et al. 1998, AJ, 116, 1009
- Scalzo, R. A., Aldering, G., Antilogus, P., et al. 2010, ApJ, 713, 1073
- Scalzo, R. A., Aldering, G., Antilogus, P., et al. 2012, ApJ, 757, 12
- Scalzo, R. A., Aldering, G., Antilogus, P., et al. 2014, MNRAS, in press (arXiv:1402.6842)
- Schlafly, E. F., & Finkbeiner, D. P. 2011, ApJ, 737, 103
- Seitzzahl, I., Ciaraldi-Schoolmann, F., Röpkke, F. K., et al. 2013, MNRAS, 429, 1156
- Shen, K., Bildsten, L., Kasen, D., et al. 2012, ApJ, 748, 35
- Silverman, J. M. et al. 2011, MNRAS, 410, 585
- Silverman, J. M. et al. 2012, MNRAS, 425, 1789
- Silverman, J. M., Nugent, P., Gal-Yam, A., et al. 2013, ApJ, 772, 125
- Silverman, J. M., Nugent, P., Gal-Yam, A., et al. 2013, ApJS, 207, 3
- Stetson, P. B. 1987, PASP, 99, 191
- Sternberg, A., Gal-Yam, A., Simon, J. D., et al. 2011, Science, 333, 856
- Stritzinger, M., Phillips, M. M., Boldt, L., et al. 2011, AJ, 142, 156
- Swartz, D. A., Sutherland, P. G., & Harkness, R. P. 1995, ApJ, 446, 766
- Taddia, F., Stritzinger, M. D., Phillips, M. M., et al. 2012, A&A, 545, 7
- Tanaka, M., Kawabata, K., Yamanaka, M., et al. 2010, ApJ, 714, 1209
- Taubenberger, S., Benetti, S., Childress, M. et al. 2011, MNRAS, 412, 2735
- Taubenberger, S., Kromer, M., Hachinger, S. et al. 2013, MNRAS, 432, 3117
- Tody, D. 1993, *Astronomical Data Analysis Software and Systems II*, 52, 173
- Thomas, R. C., Nugent, P. E., & Meza, J. C. 2011, PASP, 123, 237
- Tripp, R. 1998, A&A, 331, 815
- Wang, X., Filippenko, A. V., Ganeshalingam, M., et al. 2009, ApJ, 699, L139
- Woosley, S. E. & Weaver, T. A. 1994, ApJ, 423, 371
- Yamanaka, M., Kawabata, K., Kinugasa, K., et al. 2009, ApJ, 707, L118
- Yaron, O., & Gal-Yam, A. 2012, PASP, 124, 668
- Yuan, F., Quimby, R. M., Wheeler, J. C., et al. 2010, ApJ, 715, 1338